

1 **Isotopic composition of convective rainfall in the inland tropics of** 2 **Brazil**

3 Vinicius dos Santos¹, Didier Gastmans¹, Ana María Durán-Quesada², Ricardo Sánchez-Murillo³,
4 Kazimierz Rozanski⁴, Oliver Kracht⁵ and Demilson de Assis Quintão⁶.

5

6 ¹São Paulo State University (UNESP), Environmental Studies Center. Av. 24A Based, 1515, Bela Vista, 13.506-900, Rio Claro,
7 São Paulo, Brazil. vinicius.santos16@unesp.br; didier.gastmans@unesp.br

8 ²Escuela de Física & Centro de Investigación en Contaminación Ambiental & Centro de Investigaciones Geofísicas,
9 Universidad de Costa Rica, San José 11501, Costa Rica. ana.duranquesada@ucr.ac.cr

10 ³University of Texas at Arlington, Department of Earth and Environmental Sciences, 500 Yates Street, Arlington, Texas 76019,
11 USA. ricardo.sanchezmurillo@uta.edu

12 ⁴Faculty of Physics and Applied Computer Science, AGH University of Krakow, al. Mickiewicza 30, 30-059 Krakow, Poland.
13 rozanski@agh.edu.pl

14 ⁵International Atomic Energy Agency, Isotope Hydrology Section, Vienna International Centre, P. O. Box 100, 1400 Vienna,
15 Austria. O.Kracht@iaea.org

16 ⁶São Paulo State University (UNESP), IPMet/Science College, Est. Mun. José Sandrin IPMET, S/N, 17.048-699, Bauru, São
17 Paulo, Brazil. demilson.quintao@unesp.br

18

19 *Correspondence to:* Didier Gastmans (didier.gastmans@unesp.br)

20 **Abstract.** Strong convective systems characterize the tropical central-southern region of Brazil. These systems provide
21 abundant water supply for agro-industrial activities and pose flood risks to large cities. Here, we present high-frequency (2-10
22 min; inter and intra-event) rainfall isotopic compositions (n=90 samples) to reveal regional and local atmospheric processes
23 controlling the isotopic variability of convective systems between 2019-2021. Inter-events rainfall weighted-average (δ_{wgd})
24 values were low ($\delta^{18}\text{O}_{\text{wgd}} \leq -10.0 \text{ ‰}$) due to the influence of evapotranspiration from the Amazon forest during the summer
25 and associated with higher rainfall along Hysplit trajectories. In contrast, during autumn and spring seasons Hysplit trajectories
26 from the Atlantic Ocean and South Brazil exhibited lower rainfall amounts, resulting in high $\delta^{18}\text{O}_{\text{wgd}} \geq -4.2 \text{ ‰}$. This strong
27 regional δ_{wgd} pattern often masks intra-event isotopic variability. Therefore, we analyzed the vertical structure of local rainfall
28 using reflectivity (Z) from micro radar data. Variations in Z indicate that microphysical processes within falling raindrops led
29 to changes in $\delta^{18}\text{O}$ and *d*-excess. Our findings establish a novel framework for evaluating the meteorological controls on the
30 isotopic variability of convective precipitation in tropical South America, fill the gap of high-frequency studies in this region,
31 and generate an isotopic dataset for convective model evaluations.

32 1 Introduction

33 The tropical central-southern region of Brazil (CSB) is the primary contributor to the country's economy, with
34 agriculture and agroindustry as the main sectors (Zilli et al., 2017). These economic activities are highly dependent on seasonal
35 rainfall for irrigation and hydropower supply (Luiz Silva et al., 2019). Projected changes in the frequency of heavy and extreme
36 rainfall events (Marengo et al., 2020; Donat et al., 2013; IPCC, 2021; Marengo et al., 2021) pose a significant threat to regional
37 economic growth and energy generation. Similarly, according to Marengo et al. (2021), simulations with pre-CMIP6 models
38 suggest that the intensification of heavy rainfall events could exacerbate the prevalence of floods and landslides in susceptible
39 regions. Such occurrences have resulted in a total cost of US\$41.7 billion over the past half-century (Marengo et al., 2020;
40 World Meteorological Organization, 2021).

41 Extreme precipitation events are linked to convective systems (CS). These systems significantly contribute to the annual
42 rainfall budget and account for a large number of extreme rainfall events (Roca and Fiolleau, 2020). Across the tropics, diurnal
43 surface heating amplifies convection, generating short-lived events that can occur in consecutive days. Rapid upward
44 movement of air results in large condensation and precipitation rates (Breugem et al., 2020; Kastman et al., 2017; Lima et al.,
45 2010; Machado et al., 1998). This is identified by vigorous vertical development in the form of *cumulus-nimbus* and *cumulus*
46 *congestus* (convective clouds) and low-level divergence (stratiform clouds) (Siqueira et al., 2005; Machado and Rossow, 1993;
47 Zilli et al., 2017; Houze, 1989, 2004). Precipitation associated with these systems are commonly referred as convective and
48 stratiform rainfall, and account for 45% and 46% of the total rainfall in South America, respectively (Romatschke and Houze,
49 2013).

50 Whether rainfall is convective or stratiform has been suggested to determine variations in stable isotope composition of
51 precipitation across the tropics (Zwart et al., 2018; Sánchez-Murillo et al., 2019; Sun et al., 2019; Han et al., 2021; Aggarwal
52 et al., 2016; Munksgaard et al., 2019). Processes driving the variations in the isotopic composition in CS are more complex
53 and less understood compared to other precipitation producing systems. Studies using the isotopic composition of rain and
54 water vapor have quantified and modelled physical processes related to convection (Bony et al., 2008; Kurita, 2013). Previous
55 studies have suggested that the isotopic composition of CS is connected to the integrated history of convective activity (Risi
56 et al., 2008; Moerman et al., 2013), depth of organized convection and aggregation (Lawrence et al., 2004; Lekshmy et al.,
57 2014; Lacour et al., 2018; Galewsky et al., 2023), microphysical processes within clouds (Aggarwal et al., 2016; Lawrence et
58 al., 2004; Zwart et al., 2018), and cold pool dynamics (Torri, 2021). These interpretations simplified and lumped the effects of
59 multiple rainfall timescales (e.g. monthly, daily and sub-hourly), providing different perspectives on convective processes,
60 such as the regional (synoptic forcings) and local factors (e. g. microphysical processes occurring both within and below the
61 cloud) (Kurita et al., 2009; Muller et al., 2015; Graf et al., 2019; Lee and Fung, 2008)..

62 High-frequency rainfall sampling and analyses of stable isotope ratios has been used to better understand the evolution of
63 large weather systems such as tropical cyclones and typhoons (Sun et al., 2022; Sánchez-Murillo et al., 2019; Han et al., 2021),
64 squall lines (Taupin et al., 1997; Risi et al., 2010; Tremoy et al., 2014; de Vries et al., 2022), mid-latitude cyclones, and cold

65 fronts (Barras and Simmonds, 2009; Celle-Jeanton et al., 2004; Aemisegger et al., 2015; Thurnherr and Aemisegger, 2022;
66 Muller et al., 2015; Landais et al., 2023). High-resolution isotope information can provide a better insight into the isotopic
67 variability during the life cycle of rainfall events (Coplen et al., 2008; Muller et al., 2015; Celle-Jeanton et al., 2004).

68 In this study, we used high-frequency rainfall sampling to disentangle regional (moisture origin/transport, regional
69 atmospheric circulation) from local (below-cloud processes, vertical structure of rainfall, cloud top temperature) processes
70 controlling the isotopic composition of convective rainfall. High-frequency rainfall was integrated with ground-based
71 observational data (Micro Rain Radar and automatic weather station), satellite imagery (GOES-16), ERA-5 reanalysis
72 products, and HYSPLIT trajectories to better characterize convective rainfall over the inland tropics of Brazil.

73 **2 Data and Methods**

74 **2.1 Sampling site and weather systems**

75 The rainfall sampling site was located in Rio Claro city, São Paulo State (Fig. 1a). The station (-22.39°S, -47.54°W, 670 m
76 a.s.l.) is part of the Global Network of Isotopes in Precipitation network (GNIP) and is influenced by weather systems
77 responsible for rainfall variations and seasonality linked to the regional atmospheric circulations across the CSB region. The
78 rainfall seasonality over CSB is associated with: (i) frontal systems (FS), represented mainly by cold fronts from southern
79 South America acting throughout the year, and (ii) the activity of the South Atlantic Convergence Zone (SACZ) during austral
80 summer (December to March) (Kodama, 1992; Garreaud, 2000) (Fig. 1b). These features are mostly responsible for CS
81 development (Romatschke and Houze, 2013; Siqueira et al., 2005; Machado and Rossow, 1993) (Fig. 1c), and were captured
82 during their passage over the Rio Claro station.

83 **2.2 Rainfall sampling and isotope analyses**

84 High-frequency rainfall sampling was conducted using a passive collector (2 to 10 minutes intervals) from September 2019 to
85 February 2021, except for April, July, and August (during winter 2020), when no rainfall was observed in the study area. The
86 pandemic Covid-19 disrupted access to the university campus, thereby reducing the number of rainfall events sampled during
87 the spring of 2020, particularly at night (e.g., lockdowns). In this study, the rainfall samples collected do not consist of
88 consecutive day-night pairs during the same day. In total, 90 samples representing eight convective events (3 night-time and 5
89 day-time events) were collected. Samples were transferred to the laboratory and stored in 20 mL HDPE bottles at 4°C. In
90 parallel to high-frequency sampling, monthly cumulative rainfall samples were also collected using the methodology
91 recommended by the International Atomic Energy Agency (IAEA, 2014).

92 Rainfall samples were analyzed for stable isotope composition using Off-Axis Integrated Cavity Output Spectroscopy (Los
93 Gatos Research Inc.) at the Hydrogeology and Hydrochemistry laboratory of UNESP's Department of Applied Geology and

94 at the Chemistry School of the National University (UNA, Heredia, Costa Rica). All results are expressed in per mil relative
95 to Vienna Standard Mean Ocean Water (V-SMOW). The certified calibration standards used in UNESP were USGS-45 ($\delta^2\text{H}$
96 = -10.3‰ , $\delta^{18}\text{O} = -2.24\text{‰}$), USGS-46 ($\delta^2\text{H} = -236.0\text{‰}$, $\delta^{18}\text{O} = -29.80\text{‰}$), including one internal standard (Cachoeira de
97 Emas - CE – $\delta^2\text{H} = -36.1\text{‰}$, $\delta^{18}\text{O} = -5.36\text{‰}$). USGS standards were used to calibrate the results on the V-SMOW2-SLAP2
98 scale, whereas CE was used for memory and drift corrections. At UNA, the certified standards MTW ($\delta^2\text{H} = -130.3\text{‰}$, $\delta^{18}\text{O}$
99 = -16.7‰), USGS45 ($\delta^2\text{H} = -10.3\text{‰}$, $\delta^{18}\text{O} = -2.2\text{‰}$), and CAS ($\delta^2\text{H} = -64.3\text{‰}$, $\delta^{18}\text{O} = -8.3\text{‰}$) were used to correct the
100 measurement results for memory and drift effects and to calibrate them on the V-SMOW2-SLAP2 scale (García-Santos et al.,
101 2022). The analytical uncertainty (1σ) was 1.2‰ for $\delta^2\text{H}$ and 0.2‰ for $\delta^{18}\text{O}$ for UNESP analysis and 0.38‰ for $\delta^2\text{H}$ and
102 0.07‰ for $\delta^{18}\text{O}$ for UNA analysis. Deuterium excess (*d*-excess) was calculated as: $d\text{-excess} = \delta^2\text{H} - 8*\delta^{18}\text{O}$ (Dansgaard,
103 1964), with uncertainties (1σ) of 1.33 and 0.43‰ , respectively. This secondary isotope parameter was used to interpret the
104 influence of moisture origin/transport (Sánchez-Murillo et al., 2017; Froehlich et al., 2002) and local processes (Aemisegger
105 et al., 2015; Muller et al., 2015; Celle-Jeanton et al., 2004).

106 **2.3 Meteorological data**

107 An Automatic Weather Station (AWS) Decagon Em50 (METER) was installed next to the Micro Rain Radar (MRR) (METEK)
108 at 670 m.a.s.l, within immediate vicinity of the rainfall collection site. Meteorological data were recorded at 1 min intervals
109 for rain rate (RR, mm min^{-1}), air temperature (T, $^{\circ}\text{C}$) and relative humidity (RH, %). The MRR data for reflectivity (Z, in dBZ),
110 and fall velocity (w , m s^{-1}) were also recorded at 1 min intervals. MRR parameters correspond to the mean values measured at
111 the elevation between 150 and 350 meters above surface. MRR operated at a frequency of 24.230 GHz, modulation of 0.5 –
112 15 MHz according to the height resolution mode. For this work, different height resolutions (31 range bin) were tested, 150
113 m, 200 m, 300 m and 350 m, resulting in vertical profiles of 4650 m, 6200 m, 9300 m and 10.850 m, respectively (Endries et
114 al., 2018). The MRR data used in the following discussion are the near-surface data (first measurement from 150 m to 350 m).
115 Lifting Condensation Level (LCL, meters) was computed from AWS RH and T, using expression proposed by Soderberg et
116 al. (2013). The rainfall amount (R, mm) was also calculated during the sampling interval. GOES-16 imagery was used to
117 identify the convective nuclei of the cloud-top ($10.35\text{-}\mu\text{m}$, Band-13) and brightness temperature (BT, $^{\circ}\text{C}$), at 10 min intervals
118 during the sampling period (Ribeiro et al., 2019; Schmit et al., 2017). The $10.35\text{-}\mu\text{m}$ BT is often used to estimate the convective
119 cloud depth, since the lower BT is linked to deeper cloud tops (Adler and Fenn, 1979; Roberts and Rutledge, 2003; Adler and
120 Mack, 1986; Ribeiro et al., 2019; Machado et al., 1998). The weather systems (fronts, instabilities, and low pressure) were
121 defined according to the synoptic chart and meteorological technical bulletin of the Center for Weather Forecast and Climatic
122 Studies of the National Institute of Space Research (CPTEC/INPE) that used information of numerical models, automatic
123 weather stations, satellite and radar images, reanalysis data and regional atmospheric models, such as the Brazilian Global
124 Atmospheric Model and ETA model.

125

126 **2.4 Hysplit modeling and Reanalysis data**

127 The origin of air masses and moisture transport to the Rio Claro site were evaluated using the HYSPLIT (Hybrid-Single
128 Particle Lagrangian Integrated Trajectory) modeling framework (Stein et al., 2015; Soderberg et al., 2013). The trajectories of
129 the air masses were estimated for 240 hours prior to rainfall onset, considering the estimated time of residence of the water
130 vapor (Gimeno et al., 2010, 2020; van der Ent and Tuinenburg, 2017). Start time of trajectories was the same as the start time
131 of rainfall events. The trajectories were computed using NOAA's meteorological data (global data assimilation system, GDAS:
132 1 degree, global, 2006-present), with ending elevations of the trajectories at 1500 m above the surface, taking into account the
133 climatological height of the Low Level Jet, within 1000–2000 m (Marengo et al., 2004). Ten-day trajectories representing
134 convective events were calculated as trajectory ensembles, each consisting of twenty-seven ensemble members released at
135 start hour of convective rainfall sample collection. Ensembles were produced by varying the initial trajectory wind speeds and
136 pressures, according to the HYSPLIT ensemble algorithm, in order to account for the uncertainties involved in the simulation
137 of individual backward trajectories (Jeelani et al., 2018). A sum of the rainfall intensity (mm hr^{-1}) along the trajectories was
138 used to analyse rainout of the moist air masses according to the Jeelani et al. (2018).

139 Reanalysis data were used to better understand the influence of atmospheric circulation on isotopic composition of rainfall
140 at the study area. ERA-5 information was used to evaluate hourly vertical integrals of eastward water vapor flux ($\text{kg m}^{-1} \text{s}^{-1}$)
141 during convective events sampled. The Global Modeling and Assimilation Office (GMAO) data (MERRA-2, 1 hour, 0.5 x
142 0.625 degree, V5.12.4 were used for calculations of latent heat flux (LHF). Aqua/AIRS L3 Daily Standard Physical Retrieval
143 (AIRS-only) data (1-degree x 1-degree V7.0, Greenbelt, MD, USA, Goddard Earth Sciences Data and Information Services
144 Center) (known as GES DISC) were used for average outgoing longwave radiation (OLR). OLR values below 240 W m^{-2}
145 indicate organized deep convection (Gadgil, 2003).

146 **2.5 Identification of convective rainfall events and vertical variations of reflectivity**

147 In general, the identification of CS was based on the vertical structure of the given precipitation system (lack of the
148 melting layer and bright band - BB) in the radar profiles featuring high reflectivity values ($Z > 38 \text{ dBZ}$) (Houze, 1993, 1997;
149 Steiner and Smith, 1998; Rao et al., 2008; Mehta et al., 2020; Endries et al., 2018) and satellite imagery (Vila et al., 2008;
150 Ribeiro et al., 2019; Siqueira et al., 2005; Machado et al., 1998). Consequently, convective rainfall was defined in this study
151 by (i) convective cloud nuclei observed in GOES-16 imagery, (ii) no BB detected, (iii) $Z > 38 \text{ dBZ}$ near to the surface and (iv)
152 rainfall intensity (AWS) of at least 10 mm h^{-1} (Klaassen, 1988) (Fig. 1c,d). The convective nuclei were identified using GOES-
153 16 imagery, determined as a contiguous area of at least 40 pixels with BT lower than 235K ($\leq -38 \text{ }^\circ\text{C}$) over Rio Claro station,
154 according to previous studies (Ribeiro et al., 2019).

155 The Z is defined as the mean number of raindrops within a specific diameter interval per unit volume of air. Therefore, Z
156 represents the concentration of a particular raindrop property (in this case, the 6th power of their diameter, proportional to the

157 square of their volume) (Houze, 1993; Mehta et al., 2020; Uijlenhoet, 2001). A high Z value indicates a high concentration of
158 raindrops. A modification in the formation mechanism for precipitation particles results in a change in Z of the vertical profile
159 (Houze, 1997). Descriptive statistics were conducted on the Z values at different heights to comprehend and quantify the
160 dynamics of rain particle formation during intra-events. The resulting parameters from considering the entire vertical profile
161 of the MRR are: Z_{\max} : is the maximum reflectivity value in the vertical profile indicating the maximum concentration of
162 raindrops; Z_{median} : refers to the median reflectivity in the vertical profile and was used to synthesize the change in vertical Z
163 values; and $Z_{\text{amplitude}}$ (Z_{ampl}) is defined as the difference between the maximum and minimum reflectivity values in the vertical
164 profile. In other words, a larger Z_{ampl} indicates that raindrops undergo more microphysical transformations as they fall to the
165 surface.

166 2.6 Statistical tests

167 The Shapiro-Wilk test was applied to verify that the data distribution was normal (parametric) or non-normal (non-
168 parametric) (Shapiro, S. S.; Wilk, 1965). A significant difference (p-value < 0.05) indicates a non-parametric distribution. A
169 Spearman rank correlation test was used for nonparametric distribution data, whereas Pearson's linear correlation test was
170 applied for parametric data. Correlation tests were conducted between isotopes ($\delta^{18}\text{O}$ and d -excess) and meteorological data
171 (AWS and MRR variables) during the same time interval and from individual events. Correlation tests were not applied to
172 GOES-16 BT and reanalysis data due to their temporal resolution, which reduced the number of samples. All tests were
173 performed with significance levels defined by a p-value < 0.05, using the R statistical package (R Core Team, 2023).

174 Rainfall weighted averages were calculated for each event to evaluate large-scale processes using the equation:

$$175 \delta_{\text{wgd}} = \frac{\sum_{i=1}^n Ri\delta_i}{\sum_{i=1}^n Ri} \quad (1)$$

176 where δ_{wgd} is the rainfall weighted average of the isotopic composition, R_i is the rainfall of the event (mm), δ_i is the isotopic
177 composition of an individual sample (‰), and n is the number of samples from each event. Rainfall weighted averages refers
178 to the $\delta^{18}\text{O}_{\text{wgd}}$, $\delta^2\text{H}_{\text{wgd}}$ and d_{wgd} , and median of the $\delta^{18}\text{O}_{\text{med}}$, $\delta^2\text{H}_{\text{med}}$ and d_{med} .

179 3 Results

180 3.1 Inter-event variability of meteorological and isotopic parameters

181 3.3.1. Seasonal-mean climatic and isotopic conditions

182 The isotopic composition of monthly rainfall exhibits clear seasonal variations between September 2019 and February 2021
183 (Fig. 2a). Seasonal variability was characterized by wet (low $\delta^{18}\text{O}$) and dry (high $\delta^{18}\text{O}$) seasons (austral summer and autumn-
184 spring, respectively). Summer months were characterized by the influence of convective activity, reflected in high latent heat
185 flux and lower OLR (Fig. 2 b-d). During autumn and spring, significant lower latent heat flux and higher OLR were associated
186 with less convective development (Houze, 1997, 1989). The formation of convective rainfall may not be primarily controlled
187 by diurnal thermal convection, as rainfall is more likely to be associated with frontal systems (Siqueira and Machado, 2004),
188 as observed in the rainfall episodes during autumn and spring.

189 A significant influence of the cold fronts was observed before, during, and after their passage over the study area (Fig. 2a).
190 During autumn and spring, the convective events of 2019/11/05, 2020/11/18, and 2020/05/23 were associated with cold fronts
191 in the study area. On 2020/06/09, changes in the regional atmosphere over the state of São Paulo caused convective rainfall
192 due to an instability (frontal) system resulting from a cold front settling over the southern region of Brazil. During the summer
193 season, convective rainfall also occurred on 2020/02/01 and 2021/02/24 due to cold fronts and instability (frontal),
194 respectively. In addition, the thermal convection over land, lead to convective rainfall event on 2020/01/30. As a result of the
195 interaction between thermal convection and the incursion of the frontal system, a low-pressure system (frontal) was responsible
196 for the convective rainfall event on 2020/02/10.

197 3.3.2. Isotopic and local meteorological variations

198 Table 1 presents an overview of the sampling, isotope compositions (δ_{med} and δ_{wgd}) and median values of meteorological
199 variables from individual events. The duration of sampled events ranged from 141 min to 18 min. The T and T_{wd} exhibited
200 small differences among the events. In contrast, RR, RH, LCL, Z, w, and BT varied considerably between events. The
201 maximum recorded values for these parameters were 97%, 489 m, 46 dBZ, 8 m s⁻¹ and -63 °C, respectively. Isotope values
202 varied among convective events, with a range of -11.0 ‰, -91.2 ‰ and +15.7 ‰ for $\delta^{18}\text{O}_{\text{med}}$, $\delta^2\text{H}_{\text{med}}$ and d_{med} , respectively
203 (Table 1).

204 3.1.3. Moisture origin

205 The sourcing of moisture for rainfall over Rio Claro varies seasonally and spatially, suggesting complex interactions
206 in moisture transport and mixing that strongly influence the δ_{wgd} isotopic composition of rainfall throughout the year (Table
207 1). Hysplit air mass back-trajectories revealed three main domains as moisture origin during the presence of convective rainfall:
208 Amazon forest, Atlantic Ocean, and southern Brazil (Fig. 3).

209 Summer rainfall events were characterized by the trajectory and length of moist air masses arriving from the Amazon forest
210 (2020/02/10, 2020/02/01, and 2020/01/30) (Fig. 3a). As a result, there was a large amount of rainfall along Hysplit trajectories.

211 Rainfall amounts were 177 mm, 126 mm and 78 mm, respectively. Remarkably, these events exhibited similar isotope
212 characteristics ($\delta^2\text{H}_{\text{wgd}}$, $\delta^{18}\text{O}_{\text{wgd}}$) (Table 1). In contrast, the event on 2021/02/24 presented higher δ_{wgd} values, reflecting the
213 oceanic moisture influence (Fig. 3a), with a lowest amount of rainfall (53 mm) along Hysplit trajectory.

214 Based on ERA-5, the vertically integrated eastward vapor flux corroborates the influence of a distinct mechanism for
215 moisture transport and δ_{wgd} values. Negative values for vertical vapor fluxes over the Amazon forest during sampled convective
216 events in summer (Fig. 4a, b, d) clearly illustrate a westward moisture flux from the Atlantic Ocean to the Amazon forest.
217 Positive values in the central-southern region of Brazil indicate moisture being transported eastward from the Amazon forest.
218 However, these moisture fluxes were not observed on 2021/02/24 when the eastward vapor flux was positive with high values
219 over the Atlantic Ocean ($250 \sim 750 \text{ kg m}^{-1} \text{ s}^{-1}$).

220 The autumn convective events on 2020/05/23 and 2020/06/09 revealed a significant continental origin of moist air masses
221 (from south-western Brazil). In addition, during the second event, the Amazon-type trajectory started in the southern Atlantic
222 and did not reach the boundary of the rainforest (Fig. 3b). Both autumn events reported the lowest rainfall amounts (4 mm)
223 along Hysplit trajectories. On 2020/05/23 negative vertical flux values ($-500 \sim -250 \text{ kg m}^{-1} \text{ s}^{-1}$) were observed in south-western
224 Brazil, indicating moisture transport from the Atlantic Ocean to the continent. This favored a vapor flux ($500 \sim 750 \text{ kg m}^{-1} \text{ s}^{-1}$)
225 from western Brazil to the study area (Figure 4f). On 2020/06/09, there were slightly negative values ($-250 \sim 0 \text{ kg m}^{-1} \text{ s}^{-1}$) of
226 eastward vapor flux in the Amazon forest, indicating less influence from rainforest moisture. Conversely, positive vapor flux
227 values ($250 \sim 500 \text{ kg m}^{-1} \text{ s}^{-1}$) were observed in the western part of continental Brazil.

228 Two events in the spring season (Fig. 3c) also showed contrasting origin of moisture and d_{wgd} values, despite only slight
229 differences in $\delta^{18}\text{O}_{\text{wgd}}$ (Table 1). The mean trajectory on 2020/11/18 clearly belongs to the Amazon category, although it only
230 passed over the south-eastern boundary of the Amazon rainforest and had a much shorter length and lower rainfall along
231 Hysplit trajectory (23 mm) compared to the Amazon trajectories observed during the summer season. Thus, positive values of
232 the eastward vapor flux ($250 \sim 750 \text{ kg m}^{-1} \text{ s}^{-1}$) were not distributed along the Amazon forest to the Atlantic Ocean as typically
233 observed (Fig. 4h). The mean trajectory on 2019/11/05 the eastward vapor flux ($> 500 \text{ kg m}^{-1} \text{ s}^{-1}$, Fig. 4g) were circling around
234 Rio Claro, indicating the continental moisture origin (from southern Brazil), and low amount of rainfall along Hysplit trajectory
235 of 8 mm.

236 3.2 Intra-event variability of the isotope and meteorological parameters

237 The temporal evolution of isotope characteristics and selected meteorological parameters of convective rainfall are
238 shown in Fig. 5-6 (summer), Fig. 7 (autumn) and Fig. 8 (spring). The vertical Z variation of the MRR in all events shows a
239 pattern of values ranging from 0 to 10 dBZ at the top, a wide band of lowest values and noise attenuating the reflectivity
240 producing white horizontal and vertical bands, and an increase in Z values closer to the surface where Zmax occurs (highest
241 values ranging from 44 to 51 dBZ). During intra-events, Z, isotopic parameters, and GOES-16 BT display distinct temporal

242 patterns across events and seasons. There are large variations in Z values and inverse patterns between $\delta^{18}\text{O}$ and *d*-excess
243 (more variable), and between T and RH. Different decreasing, increasing or stable trends were observed in BT values. The
244 following sections described the main seasonal results for the intra-event analysis.

245 3.2.1. During summer

246 Low variability patterns were observed on 2020/02/01 and 2020/01/30 (Fig.5) for $\delta^{18}\text{O}$, T, RH, and BT. Both events
247 were shorter in duration (≤ 25 minutes) and had a higher R (≤ 5.4 mm) value at the beginning, which decreased over the course
248 of the event (0.2 mm). Similar MRR vertical profiles were observed between the events, illustrated by similar Z values, with
249 low variability of Zmedian (7 ~ 17 dBZ and 8 ~ 15 dBZ), Zmax (23 ~ 48 dBZ and 19 ~ 46 dBZ) and Z amplitude decreasing
250 along the event (17 ~ 45 dBZ and 19 ~ 42 dBZ), respectively. Strong and significant ($p < 0.0001$) correlations were observed
251 between isotopic composition and MRR parameters for 2020/02/01: $\delta^{18}\text{O}$ -Z ($r = -0.9$), $\delta^{18}\text{O}$ -w ($r = -0.9$), $\delta^{18}\text{O}$ -Zmáx ($r = -0.9$),
252 $\delta^{18}\text{O}$ -Zampl ($r = -0.8$), *d*-excess-Z ($r = 0.9$), *d*-excess-w ($r = 0.9$), *d*-excess-Zmax ($r = -0.9$) and *d*-excess-Zampl ($r = 0.9$). No
253 significant correlations between isotopic composition and meteorological parameters for 2020/01/30, except for a moderate
254 correlation between $\delta^2\text{H}$ and Zmedian ($r = -0.5$).

255 Large isotopic and meteorological variations were observed for 2021/02/24 ($\delta^{18}\text{O}$: -7.9 ~ -4.4 ‰, *d*-excess: +1.2 to
256 +18.4 ‰) and 2020/02/10 ($\delta^{18}\text{O}$: -15.2 ~ -7.9 ‰, *d*-excess: +4.8 ~ +21.4 ‰.) (Fig. 6). On 2021/02/24 a strong and significant
257 ($p < 0.05$) correlation was observed between $\delta^{18}\text{O}$ and R ($r = -0.8$), Z ($r = -0.6$), Zmax ($r = -0.6$), Zampl ($r = -0.6$), Zmedian (r
258 = 0.7), and between *d*-excess and R ($r = -0.6$), Z ($r = -0.5$), Zmax ($r = 0.5$), Zampl ($r = 0.5$) and Zmedian ($r = -0.7$). For
259 2020/02/10, significant correlations were reported between $\delta^{18}\text{O}$ -RH ($r = -0.5$), *d*-excess-RH ($r = 0.5$) and *d*-excess and
260 Zmedian ($r = 0.5$). In addition, *d*-excess values lower than +10‰ were observed at the end of the events (2020/02/01,
261 2020/02/10 and 2021/02/24), corresponding to low values of the R and Z parameters and high RH (black dotted cycle in Figs.
262 5 and 6).

263 3.2.2 During autumn and spring

264 Autumn events show distinct isotopic patterns. The 2020/05/23 event exhibited a small isotopic ($\delta^{18}\text{O}$: -2.6 ~ -2.7 ‰,
265 *d*-excess: +16.7 ~ +19.0 ‰) and meteorological (declining T, R and Z parameters along the event) variation (Fig. 7). On
266 2020/06/09 (Fig. 7) two isotopic distribution patterns were recorded, with minimal ($\delta^{18}\text{O}$: -3.6 ~ -3.4 ‰, *d*-excess: +26.4 ~
267 +17.7 ‰) and large ($\delta^{18}\text{O}$: -1.5 ~ -2.9 ‰; *d*-excess: +15.3 ~ +6.3 ‰) variations, corresponding to high RH, R, Zampl and
268 Zmax (grey bands in Fig. 8). Strong and significant ($p < 0.05$) correlations were observed between $\delta^{18}\text{O}$ -RH ($r = 0.5$), $\delta^{18}\text{O}$ -T
269 ($r = -0.6$), *d*-excess-RH ($r = -0.6$), *d*-excess-T ($r = 0.7$) and *d*-excess- Zampl ($r = -0.5$) on 2020/06/09. However, no significant
270 correlations were found during the event on 2020/05/23.

271 Distinctive isotopic patterns were also found during spring events. On 2019/11/05, a change in the vertical profile
272 and Z parameters was observed (grey bands in Fig. 8), with a shift in $\delta^{18}\text{O}$ from maximum depletion (-4.1 ‰) to enrichment
273 at the end of the event (-3.2 ~ -1.7 ‰). On 2020/11/18, there was a gradual decrease observed in $\delta^{18}\text{O}$ (-2.7 ~ -5.4 ‰) and an
274 increase in *d*-excess (+10.2 ~ +23.1 ‰). The latter was accompanied by a progressive increase in RH, decrease in T, and
275 constant Zmedian values (Fig. 8). On 2019/11/05 a strong and significant ($p < 0.005$) correlations were observed between $\delta^{18}\text{O}$
276 and Z ($r = -0.7$), w ($r = -0.7$), Zmax ($r = -0.7$) and Zamp1 ($r = -0.6$), and between *d*-excess and RH ($r = -0.7$), T ($r = 0.8$), w (r
277 = 0.6), Zamp1 ($r = 0.5$) and Zmedian ($r = -0.5$). For 2020/11/18, significant correlations were obtained between $\delta^{18}\text{O}$ -RH ($r =$
278 -0.5), $\delta^{18}\text{O}$ -T ($r = 0.7$), *d*-excess-Zamp1 ($r = 0.7$).

279 4. Discussion

280 Detailed evaluations of the isotopic variability in convective rainfall were provided at both inter- and intra-event
281 scales. The key regional and local controls on the isotopic composition of convective rainfall can be divided in two groups: (i)
282 rainfall produced by different moisture source region(s) represented by inter-event isotopic values, and (ii) local effects
283 associated with vertical rainfall structure and surface meteorological conditions. In the summer, thermal conditions dominate
284 convective processes. During autumn and spring, convective rainfall was associated with frontal systems (Fig. 2). In this
285 regard, δ_{wgd} values better constrained the large-scale processes (such as vapor origin, convective activity and weather systems)
286 with stronger rainfall amount dependencies. The individual isotopic patterns influenced by local effects revealed microphysical
287 processes such as coalescence (i.e., higher concentration of raindrops with high Z values) that are often masked by weighted
288 averages and long-term averages during the evolution of individual precipitation systems.

289 4.1 Regional atmospheric controls

290 Regional aspects of atmospheric moisture transport to Rio Claro were illustrated in HYSPLIT backward trajectories
291 (Fig. 3) and maps of vertically integrated moisture flux across the region (Fig. 4). Most of moist air masses arriving at Rio
292 Claro during summer exhibited a common origin in the equatorial Atlantic Ocean and were subjected to a long rainfall rainout,
293 extending over several thousand kilometers. Along this pathway, air masses interacted with the Amazon forest. Intensive
294 moisture recycling resulted in a small continental isotope gradient across the Amazon forest (Salati et al., 1979; Rozanski et
295 al., 1993) and elevated *d*-excess (Gat, J. R., & Matsui, 1991). At Rio Claro, the arriving air masses are depleted in heavy
296 isotopes ($\delta_{\text{wgd}} \leq -10.0$ ‰) due to rainout along the trajectories (≥ 78 mm), with consistent $d_{\text{wgd}} > +14.0$ ‰, inherited through
297 the interaction of maritime moisture with the Amazon forest. In contrast, the summer event on 2021/02/24 was influenced by
298 oceanic moisture and had a short trajectory compared to other typical summer events. The convective events during spring and
299 autumn season exhibited substantially shorter trajectories suggesting that the atmospheric “pump” transporting moisture from

300 the equatorial Atlantic Ocean to the Amazon forest was much weaker or non-existent during this time of the year. Those short
301 trajectories suggest enhanced evapotranspiration of source moisture for rainfall (Salati et al., 1979; Risi et al., 2013; Gat, J. R.,
302 & Matsui, 1991; Worden et al., 2007; Brown et al., 2008; Levin et al., 2009; Worden et al., 2021). As a result, those trajectories
303 were characterized by a reduction in the amount of rainfall along the trajectories and enriched $\delta^{18}\text{O}_{\text{wgd}} = \geq -4.2 \text{ ‰}$ and higher
304 $d_{\text{wgd}} = \geq +16.5 \text{ ‰}$. In addition, the highest d_{wgd} (+23.3 ‰) observed on 2019/11/05 was characterized by a continental moisture
305 trajectory circling around Rio Claro (Fig. 3c) over a greater RH gradient (e.g., sugar cane crop regions) (da Silva et al., 2021).
306 Evaporation from soil increases kinetic fractionation, favoring the evaporation of HDO due to high diffusivity, resulting in a
307 strong d -excess changes (Risi et al., 2013).

308 4.2 Local atmospheric controls

309 In deep convection, precipitation particles primarily grow through the collection of water (known as coalescence) by
310 larger droplets and/or ice particles (known as riming). These larger particles sweep water from the cloud on their falling paths
311 in the presence of strong rising air currents. As a parcel of rising air ascends, the growing particles within it move until they
312 become large enough to fall relative to the air. As the air parcel ascends, particles fall out at each successive height. The
313 remaining lighter particles disperse laterally over a larger area due to the diverging airflow. Convective air movements create
314 concentrated reflectivity peaks in the radar pattern because most of the precipitation mass falls within a few kilometres of the
315 updraft centres (Houghton, 1968; Houze, 1997). The irregular blank bands visible in the vertical MRR profiles (Fig. 5) could
316 be attributed to the lateral dispersion of remaining particles. The concentrated high reflectivity values (Fig. 5) illustrate this
317 pattern, which typically occurs close to the surface and indicates the occurrence of Z_{max} .

318 Variations in the isotopic composition of the rainfall reflect changes in this mechanism of raindrop formation (Sun et
319 al., 2022; Aggarwal et al., 2016). This is shown by the vertical variation in the Z values of the events on 2020/02/10,
320 2021/02/24, 2020/06/09 and 2019/11/05 (grey band in Fig. 6, 7, 8). A possible reason for this change is that the process of
321 coalescence during the falling raindrops towards the surface may have been altered. This can be seen in the higher Z_{max}
322 values (40 ~ 50 dBZ), which suggest that water particles were being incorporated into the raindrop during the fall at the surface,
323 resulting in a larger water particle and consequently a higher concentration in the raindrops and the occurrence of Z_{max} close
324 to the surface. The $\delta^{18}\text{O}$ values generally increased while the d -excess decreased, resulting in a change in the isotopic variation
325 pattern, reflecting the diffusive exchange process between the surrounding vapor and the raindrops (Gedzelman and Lawrence,
326 1990; Celle-Jeanton et al., 2004). In contrast, the isotopic pattern of the events on 2020/02/01 (Fig. 5), 2020/01/30 (Fig. 5),
327 and 2020/05/23 (Fig. 7) exhibited small variation due to the low variability in Z values. Therefore, the main local control on
328 the isotopic variability of intra-events corresponded to the vertical structure of the rainfall event.

329 The d -excess values decreased and the $\delta^{18}\text{O}$ values increased at the end of the events on 2020/02/01, 2021/02/24 and
330 2020/02/10 (black dotted cycle in Figs. 5a, 6a and 6b, respectively). This was due to the formation of residual rainfall at low
331 altitudes and a decrease in rainfall intensity during the dissipation phase of the convective cell. On 2020/11/18 (Fig. 8b), the

332 $\delta^{18}\text{O}$ values constantly decreased, illustrating a typical depletion of heavy isotopes based on Rayleigh distillation processes
333 due to the progressive condensation of convective systems. Previous studies have widely observed these mechanisms during
334 intra-events, and both interpretations are supported (Adar et al., 1991; Coplen et al., 2008, 2015; Barras and Simmonds, 2009;
335 Celle-Jeanton et al., 2004; Muller et al., 2015).

336 **5 Concluding remarks**

337 This study used high-frequency isotopic composition of rainfall as well as meteorological data to investigate the
338 regional and local mechanisms controlling the isotopic characteristics of convective precipitation. Based on the inter-event
339 analysis, the regional isotopic characteristics are different between summer and autumn-spring seasons. The δ_{wgd} is determined
340 by moisture transport mechanisms and convection features. The main factors are the gradual reduction of heavy isotopes along
341 moisture trajectories. The rainfall produced along these tracks was pronounced during summer events, associated with the
342 longer moisture transport pathway from the Amazon Forest, producing depleted isotope values. In contrast, reduced autumn
343 and spring rainfall along trajectories is associated with a shorter moisture transport pathway from the Atlantic Ocean and
344 southern Brazil. This produces enriched isotope characteristics and high d_{wgd} values associated with transpiration and soil
345 evaporation along the moisture transport pathway.

346 Within convective events, the regional δ_{wgd} -signature was altered by local effects, as shown by the intra-event isotopic
347 evolution. The vertical structure of rainfall, described by the Z parameters in the vertical MRR profile, is the main local control.
348 During falling raindrops, a microphysical change can cause a vertical change in Z values, resulting in abrupt variations in
349 isotopic patterns. These findings were supported by significant and strong correlations between the MRR and isotopic
350 parameters in each event. Therefore, the isotopic composition of convective rainfall is controlled by an interplay of regional
351 and local factors. The complex and dynamic conditions of convective rainfall formation across the tropics can be understood
352 using high-frequency analysis. Although high-frequency rainfall sampling is logistically difficult, we encourage future studies
353 of this type in different geographical regions across the tropics, to better understand the factors controlling the isotopic
354 composition of convective rainfall during rainy period. Extensive monitoring of local meteorological parameters and modeling
355 of regional moisture transport to the rainfall collection site, along with the application of more robust below-cloud models,
356 should accompany such studies.

357 **Data availability**

358 A complete database (isotope characteristics of rainfall as well as selected meteorological parameters characterizing these
359 events) are available at: <https://doi.org/10.17632/kk3gs8zn4s.1> (dos Santos et al., 2023). Monthly GNIP data:
360 <https://www.iaea.org/services/networks/gnip>. GOES-16 imageries are available at:
361 https://home.chpc.utah.edu/~u0553130/Brian_Blaylock/cgi-bin/goes16_download.cgi. The weather systems are available at:

362 <https://www.marinha.mil.br/chm/dados-do-smm-cartas-sinoticas/cartas-sinoticas> and
363 <http://tempo.cptec.inpe.br/boletimtecnico/pt>. Reanalysis data are available at:
364 (<https://cds.climate.copernicus.eu/cdsapp#!/search?type=dataset>. The Global Modeling and Assimilation Office (GMAO) data
365 are available at: <https://goldsmr4.gesdisc.eosdis.nasa.gov/data/MERRA2/M2T1NXFLX.5.12.4/>).
366 Goddard Earth Sciences Data and Information Services Center (GES DISC) data are available at:
367 https://disc.gsfc.nasa.gov/datasets/AIRS3STD_7.0/summary.

368

369 *Acknowledgment*

370 FAPESP support for the scholarship provided under the Process 2019/03467-3 and 2021/10538-4 is acknowledged. Durán-
371 Quesada acknowledges time for analysis and writing provided within UCR C1038 project. The authors acknowledge Troy G.
372 for English revision.

373

374 **Financial support**

375 This work was funded by grants the São Paulo Research Foundation (FAPESP) under Processes 2018/06666-4, 2019/03467-
376 3 and 2021/10538-4, and by the International Atomic Energy Agency Grant CRP-F31006.

377 **References**

378 Adar, E. M. ., Karnieli, A. ., Sandler, B. Z. ., Issar, A. ., Wolf, M. ., and Landsman, L.: A mechanical sequential rain sampler
379 for isotopic and chemical analysis, Vienna, 32 pp., 1991.

380 Adler, R. F. and Fenn, D. D.: Thunderstorm vertical velocities estimated from satellite data, *American*, 36, 1747–1754,
381 [https://doi.org/10.1175/1520-0469\(1979\)036,1747:TVVEFS.2.0.CO;2](https://doi.org/10.1175/1520-0469(1979)036,1747:TVVEFS.2.0.CO;2), 1979.

382 Adler, R. F. and Mack, R. A.: Thunderstorm cloud top dynamics as inferred from satellite observations and a cloud top parcel
383 model, *American Meteorological Society*, 43, 1945–1960, [https://doi.org/10.1175/1520-0469\(1986\)043,1945:TCTDAI.2.0.CO;2](https://doi.org/10.1175/1520-0469(1986)043,1945:TCTDAI.2.0.CO;2), 1986.

385 Aemisegger, F. ., Spiegel, J. K. ., Pfahl, S. ., Sodemann, H. ., Eugster, W. ., and Wernli, H.: Isotope meteorology of cold front
386 passages: A case study combining observations and modeling, *Geophysical Research Letters*, 42, 5652–5660,
387 <https://doi.org/10.1002/2015GL063988>, 2015.

388 Aggarwal, P. K., Romatschke, U., Araguas-Araguas, L., Belachew, D., Longstaffe, F. J., Berg, P., Schumacher, C., and Funk,
389 A.: Proportions of convective and stratiform precipitation revealed in water isotope ratios, *Nature Geoscience*, 9, 624–629,
390 <https://doi.org/10.1038/ngeo2739>, 2016.

391 Barras, V. and Simmonds, I.: Observation and modeling of stable water isotopes as diagnostics of rainfall dynamics over
392 southeastern Australia, *Journal of Geophysical Research Atmospheres*, 114, <https://doi.org/10.1029/2009JD012132>, 2009.

393 Bony, S., Risi, C., and Vimeux, F.: Influence of convective processes on the isotopic composition ($\delta^{18}\text{O}$ and δD) of

394 precipitation and water vapor in the tropics: 1. Radiative-convective equilibrium and Tropical Ocean–Global Atmosphere–
395 Coupled Ocean-Atmosphere Response Experiment (TOGA-CO, *Journal of Geophysical Research: Atmospheres*, 113, 1–21,
396 <https://doi.org/10.1029/2008JD009942>, 2008.

397 Breugem, A. J., Wesseling, J. G., Oostindie, K., and Ritsema, C. J.: Meteorological aspects of heavy precipitation in relation
398 to floods – An overview, *Earth-Science Reviews*, 204, 103171, <https://doi.org/10.1016/j.earscirev.2020.103171>, 2020.

399 Brown, D., Worden, J., and Noone, D.: Comparison of atmospheric hydrology over convective continental regions using water
400 vapor isotope measurements from space, *Journal of Geophysical Research: Atmospheres*, 113, 1–17,
401 <https://doi.org/10.1029/2007JD009676>, 2008.

402 Celle-Jeanton, H., Gonfiantini, R., Travi, Y., and Sol, B.: Oxygen-18 variations of rainwater during precipitation: Application
403 of the Rayleigh model to selected rainfalls in Southern France, *Journal of Hydrology*, 289, 165–177,
404 <https://doi.org/10.1016/j.jhydrol.2003.11.017>, 2004.

405 Coplen, T. B., Neiman, P. J., White, A. B., Landwehr, J. M., Ralph, F. M., and Dettinger, M. D.: Extreme changes in stable
406 hydrogen isotopes and precipitation characteristics in a landfalling Pacific storm, *Geophysical Research Letters*, 35, L21808,
407 <https://doi.org/10.1029/2008GL035481>, 2008.

408 Coplen, T. B., Neiman, P. J., White, A. B., Ralph, F. M., Coplen, T. B., Neiman, P. J., White, A. B., and Ralph, F. M.: Tellus
409 B : Chemical and Physical Meteorology Categorisation of northern California rainfall for periods with and without a radar
410 brightband using stable isotopes and a novel automated precipitation collector Categorisation of northern California rainfall ,
411 0889, <https://doi.org/10.3402/tellusb.v67.28574>, 2015.

412 Dansgaard, W.: Stable isotopes in precipitation, *Tellus*, 16, 436–468, <https://doi.org/10.3402/tellusa.v16i4.8993>, 1964.

413 Donat, M. G., Alexander, L. V., Yang, H., Durre, I., Vose, R., Dunn, R. J. H., Willett, K. M., Aguilar, E., Brunet, M., Caesar,
414 J., Hewitson, B., Jack, C., Klein Tank, A. M. G., Kruger, A. C., Marengo, J., Peterson, T. C., Renom, M., Oria Rojas, C.,
415 Rusticucci, M., Salinger, J., Elayah, A. S., Sekele, S. S., Srivastava, A. K., Trewin, B., Villarroel, C., Vincent, L. A., Zhai, P.,
416 Zhang, X., and Kitching, S.: Updated analyses of temperature and precipitation extreme indices since the beginning of the
417 twentieth century: The HadEX2 dataset, *Journal of Geophysical Research Atmospheres*, 118, 2098–2118,
418 <https://doi.org/10.1002/jgrd.50150>, 2013.

419 Endries, J. L., Perry, L. B., Yuter, S. E., Seimon, A., Andrade-Flores, M., Winkelmann, R., Quispe, N., Rado, M., Montoya,
420 N., Velarde, F., and Arias, S.: Radar-observed characteristics of precipitation in the tropical high andes of Southern Peru and
421 Bolivia, *Journal of Applied Meteorology and Climatology*, 57, 1441–1458, <https://doi.org/10.1175/JAMC-D-17-0248.1>, 2018.

422 van der Ent, R. J. and Tuinenburg, O. A.: The residence time of water in the atmosphere revisited, *Hydrology and Earth System
423 Sciences*, 21, 779–790, <https://doi.org/10.5194/hess-21-779-2017>, 2017.

424 Froehlich, K., Gibson, J. J., and Aggarwal, P.: Deuterium excess in precipitation and its climatological significance, *Journal
425 of Geophysical Research-Atmospheres*, 1–23, 2002.

426 Gadgil, S.: The Indian monsoon and its variability, *Annual Review of Earth and Planetary Sciences*, 31, 429–467,
427 <https://doi.org/10.1146/annurev.earth.31.100901.141251>, 2003.

428 Galewsky, J., Schneider, M., Diekmann, C., Semie, A., Bony, S., Risi, C., Emanuel, K., and Brogniez, H.: The influence of
429 convective aggregation on the stable isotopic composition of water vapor, *AGU Advances*, 4, 1–16,
430 <https://doi.org/10.1029/2023AV000877>, 2023.

431 García-Santos, S., Sánchez-Murillo, R., Peña-Paz, T., Chirinos-Escobar, M. J., Hernández-Ortiz, J. O., Mejía-Escobar, E. J.,
432 and Ortega, L.: Water stable isotopes reveal a complex rainfall to groundwater connectivity in central Honduras, *Science of*
433 *the Total Environment*, 844, <https://doi.org/10.1016/j.scitotenv.2022.156941>, 2022.

434 Garreaud, R. D.: Cold air incursions over subtropical South America: Mean structure and dynamics, *Monthly Weather Review*,
435 128, 2544–2559, [https://doi.org/10.1175/1520-0493\(2000\)128<2544:caioss>2.0.co;2](https://doi.org/10.1175/1520-0493(2000)128<2544:caioss>2.0.co;2), 2000.

436 Gat, J. R., & Matsui, E.: Atmospheric water balance in the Amazon Basin: An isotopic evapotranspiration model, *Journal of*
437 *Geophysical Research*, 96, 13179–13188, <https://doi.org/https://doi.org/10.1029/91JD00054>, 1991.

438 Gedzelman, S. D. and Lawrence, J. R.: The Isotopic Composition of Precipitation from Two Extratropical Cyclones, *American*
439 *Meteorological Society*, 118, 495–509, [https://doi.org/10.1175/1520-0493\(1990\)118,0495:TICOPF.2.0.CO;2](https://doi.org/10.1175/1520-0493(1990)118,0495:TICOPF.2.0.CO;2), 1990.

440 Gimeno, L., Drumond, A., Nieto, R., Trigo, R. M., and Stohl, A.: On the origin of continental precipitation, *Geophysical*
441 *Research Letters*, 37, 1–7, <https://doi.org/10.1029/2010GL043712>, 2010.

442 Gimeno, L., Vázquez, M., Eiras-Barca, J., Sorí, R., Stojanovic, M., Algarra, I., Nieto, R., Ramos, A. M., Durán-Quesada, A.
443 M., and Dominguez, F.: Recent progress on the sources of continental precipitation as revealed by moisture transport analysis,
444 *Earth-Science Reviews*, 201, 103070, <https://doi.org/10.1016/j.earscirev.2019.103070>, 2020.

445 Graf, P., Wernli, H., Pfahl, S., and Sodemann, H.: A new interpretative framework for below-cloud effects on stable water
446 isotopes in vapour and rain, *Atmospheric Chemistry and Physics*, 19, 747–765, <https://doi.org/10.5194/acp-19-747-2019>,
447 2019.

448 Han, X., Lang, Y., Wang, T., Liu, C.-Q., Li, F., Wang, F., Guo, Q., Li, S., Liu, M., Wang, Y., and Xu, A.: Temporal and spatial
449 variations in stable isotopic compositions of precipitation during the typhoon Lekima (2019), China, *Science of The Total*
450 *Environment*, 762, 143143, <https://doi.org/10.1016/j.scitotenv.2020.143143>, 2021.

451 Houghton, H. G.: On Precipitation Mechanisms and their Artificial Modification, *Journal of Applied Meteorology*, 7, 851–
452 859, [https://doi.org/10.1175/1520-0450\(1968\)007<0851:OPMATA>2.0.CO;2](https://doi.org/10.1175/1520-0450(1968)007<0851:OPMATA>2.0.CO;2), 1968.

453 Houze, R.: Stratiform precipitation in regions of convection: A Meteorological Paradox?, *Bulletin of the American*
454 *Meteorological Society*, 78, 2179–2195, 1997.

455 Houze, R. A.: *Cloud dynamics*, Academic Press Limited, 573 pp., [https://doi.org/10.1016/0377-0265\(87\)90017-0](https://doi.org/10.1016/0377-0265(87)90017-0), 1993.

456 Houze, R. A.: Mesoscale Convective Systems, in: *International Geophysics*, vol. 104, 237–286, <https://doi.org/10.1016/B978-0-12-374266-7.00009-3>, 2004.

458 Houze, R. A. J.: Observed structure of mesoscale convective systems and implications for large-scale heating., *Quart. J. Roy.*
459 *Meteor. Soc.*, 115, 425–461, 1989.

460 IAEA: IAEA / GNIP precipitation sampling guide V2.02, *Global Network of Isotopes in Precipitation (GNIP)*, 20, 2014.

461 IPCC, W. G. I.-T. P. S. B.: Regional fact sheet – Central and South America, *Sixth Assessment Report*, 1–2 pp., 2021.

462 Jeelani, G., Deshpande, R. D., Galkowski, M., and Rozanski, K.: Isotopic composition of daily precipitation along the southern
463 foothills of the Himalayas: Impact of marine and continental sources of atmospheric moisture, *Atmospheric Chemistry and*
464 *Physics*, 18, 8789–8805, <https://doi.org/10.5194/acp-18-8789-2018>, 2018.

465 Kastman, J., Market, P., Fox, N., Foscatto, A., and Lupo, A.: Lightning and rainfall characteristics in elevated vs. surface based
466 convection in the midwest that produce heavy rainfall, *Atmosphere*, 8, 36, <https://doi.org/10.3390/atmos8020036>, 2017.

467 Klaassen, W.: Radar Observations and Simulation of the Melting Layer of Precipitation, *Journal of the Atmospheric Sciences*,
468 45, 3741–3753, 1988.

469 Kodama, Y.: Large-scale common features of subtropical precipitation zones (the Baiu Frontal Zone , the SPCZ , and the
470 SACZ) Part I: Characteristics of subtropical frontal zones, *Journal of the Meteorological Society of Japan*, 70, 813–836,
471 <https://doi.org/10.1248/cpb.37.3229>, 1992.

472 Kurita, N.: Water isotopic variability in response to mesoscale convective system over the tropical ocean, *Journal of*
473 *Geophysical Research Atmospheres*, 118, 10376–10390, <https://doi.org/10.1002/jgrd.50754>, 2013.

474 Kurita, N., Ichianagi, K., Matsumoto, J., Yamanaka, M. D., and Ohata, T.: The relationship between the isotopic content of
475 precipitation and the precipitation amount in tropical regions, *Journal of Geochemical Exploration*, 102, 113–122,
476 <https://doi.org/10.1016/j.gexplo.2009.03.002>, 2009.

477 Lacour, J. L., Risi, C., Worden, J., Clerbaux, C., and Coheur, P. F.: Importance of depth and intensity of convection on the
478 isotopic composition of water vapor as seen from IASI and TES δD observations, *Earth and Planetary Science Letters*, 481,
479 387–394, <https://doi.org/10.1016/j.epsl.2017.10.048>, 2018.

480 Landais, A., Agosta, C., Vimeux, F., Magand, O., Solis, C., Cauquoin, A., Dutrievoz, N., Risi, C., Leroy-Dos Santos, C.,
481 Fourré, E., Cattani, O., Jossoud, O., Minster, B., Prié, F., Casaso, M., Dommergue, A., Bertrand, Y., and Werner, M.: Abrupt
482 excursion in water vapor isotopic variability during cold fronts at the Pointe Benedicte observatory in Amsterdam Island,
483 *Atmospheric Chemistry and Physics*, Preprint, 1–33, <https://doi.org/https://doi.org/10.5194/egusphere-2023-1617>, 2023.

484 Lawrence, J. R., Gedzelman, S. D., Dexheimer, D., Cho, H., Carrie, G. D., Gasparini, R., Anderson, C. R., Bowman, K. P.,
485 and Biggerstaff, M. I.: Stable isotopic composition of water vapor in the tropics, *Journal of Geophysical Research:*
486 *Atmospheres*, 109, 16, <https://doi.org/10.1029/2003JD004046>, 2004.

487 Lee, J. and Fung, I.: “Amount effect” of water isotopes and quantitative analysis of post-condensation processes, *Hydrological*
488 *Processes*, 22, 1–8, <https://doi.org/10.1002/hyp.6637>, 2008.

489 Lekshmy, P. R., Midhun, M., Ramesh, R., and Jani, R. A.: ^{18}O depletion in monsoon rain relates to large scale organized
490 convection rather than the amount of rainfall, *Scientific Reports*, 4, 1–5, <https://doi.org/10.1038/srep05661>, 2014.

491 Levin, N. E., Zipser, E. J., and Ceding, T. E.: Isotopic composition of waters from Ethiopia and Kenya: Insights into moisture
492 sources for eastern Africa, *Journal of Geophysical Research Atmospheres*, 114, 1–13, <https://doi.org/10.1029/2009JD012166>,
493 2009.

494 Lima, K. C., Satyamurty, P., and Fernández, J. P. R.: Large-scale atmospheric conditions associated with heavy rainfall
495 episodes in Southeast Brazil, *Theoretical and Applied Climatology*, 101, 121–135, <https://doi.org/10.1007/s00704-009-0207->

496 9, 2010.

497 Luiz Silva, W., Xavier, L. N. R., Maceira, M. E. P., and Rotunno, O. C.: Climatological and hydrological patterns and verified
498 trends in precipitation and streamflow in the basins of Brazilian hydroelectric plants, *Theoretical and Applied Climatology*,
499 137, 353–371, <https://doi.org/10.1007/s00704-018-2600-8>, 2019.

500 Machado, L. A. T. and Rossow, W. B.: Structural Characteristics and Radiative Properties of Tropical Cloud Clusters, *Monthly*
501 *Weather Review*, 121, 3234–3260, 1993.

502 Machado, L. A. T., Rossow, W. B., Guedes, R. L., and Walker, A. W.: Life cycle variations of mesoscale convective systems
503 over the Americas, *Monthly Weather Review*, 126, 1630–1654, [https://doi.org/10.1175/1520-0493\(1998\)126<1630:LCVOMC>2.0.CO;2](https://doi.org/10.1175/1520-0493(1998)126<1630:LCVOMC>2.0.CO;2), 1998.

505 Marengo, J. A., Soares, W. R., Saulo, C., and Nicolini, M.: Climatology of the low-level jet east of the Andes as derived from
506 the NCEP-NCAR reanalyses: Characteristics and temporal variability, *Journal of Climate*, 17, 2261–2280,
507 [https://doi.org/10.1175/1520-0442\(2004\)017<2261:COTLJE>2.0.CO;2](https://doi.org/10.1175/1520-0442(2004)017<2261:COTLJE>2.0.CO;2), 2004.

508 Marengo, J. A., Ambrizzi, T., Alves, L. M., Barreto, N. J. C., Simões Reboita, M., and Ramos, A. M.: Changing Trends in
509 Rainfall Extremes in the Metropolitan Area of São Paulo: Causes and Impacts, *Frontiers in Climate*, 2, 1–13,
510 <https://doi.org/10.3389/fclim.2020.00003>, 2020.

511 Marengo, J. A., Camarinha, P. I., Alves, L. M., Diniz, F., and Betts, R. A.: Extreme Rainfall and Hydro-Geo-Meteorological
512 Disaster Risk in 1.5, 2.0, and 4.0°C Global Warming Scenarios: An Analysis for Brazil, *Frontiers in Climate*, 3, 1–17,
513 <https://doi.org/10.3389/fclim.2021.610433>, 2021.

514 Mehta, S., Mehta, S. K., Singh, S., Mitra, A., Ghosh, S. K., and Raha, S.: Characteristics of the Z–R Relationships Observed
515 Using Micro Rain Radar (MRR-2) over Darjeeling (27.05° N, 88.26° E): A Complex Terrain Region in the Eastern Himalayas,
516 *Pure and Applied Geophysics*, 177, 4521–4534, <https://doi.org/10.1007/s00024-020-02472-6>, 2020.

517 Moerman, J. W., Cobb, K. M., Adkins, J. F., Sodemann, H., Clark, B., and Tuen, A. A.: Diurnal to interannual rainfall $\delta^{18}O$
518 variations in northern Borneo driven by regional hydrology, *Earth and Planetary Science Letters*, 369–370, 108–119,
519 <https://doi.org/10.1016/j.epsl.2013.03.014>, 2013.

520 Muller, C. L., Baker, A., Fairchild, I. J., Kidd, C., and Boomer, I.: Intra-Event Trends in Stable Isotopes: Exploring Midlatitude
521 Precipitation Using a Vertically Pointing Micro Rain Radar, *Journal of Hydrometeorology*, 16, 194–213,
522 <https://doi.org/10.1175/JHM-D-14-0038.1>, 2015.

523 Munksgaard, N. C., Kurita, N., Sánchez-Murillo, R., Ahmed, N., Araguas, L., Balachew, D. L., Bird, M. I., Chakraborty, S.,
524 Kien Chinh, N., Cobb, K. M., Ellis, S. A., Esquivel-Hernández, G., Ganyaglo, S. Y., Gao, J., Gastmans, D., Kaseke, K. F.,
525 Kebede, S., Morales, M. R., Mueller, M., Poh, S. C., Santos, V. dos, Shaoneng, H., Wang, L., Yacobaccio, H., and Zwart, C.:
526 Data Descriptor: Daily observations of stable isotope ratios of rainfall in the tropics, *Scientific Reports*, 9, 1–7,
527 <https://doi.org/10.1038/s41598-019-50973-9>, 2019.

528 R Core Team: A language and environment for statistical computing. R Foundation for Statistical Computing, Vienna, Austria.
529 <https://www.R-project.org/>, 2023.

530 Rao, N. T., Kirankumar, N. V. P., Radhakrishna, B., and Rao, N. D.: Classification of tropical precipitating systems using
531 wind profiler spectral moments. Part I: Algorithm description and validation, *Journal of Atmospheric and Oceanic Technology*,
532 25, 884–897, <https://doi.org/10.1175/2007JTECHA1031.1>, 2008.

533 Ribeiro, B. Z., Machado, L. A. T., Biscaro, T. S., Freitas, E. D., Mozer, K. W., and Goodman, S. J.: An evaluation of the
534 GOES-16 rapid scan for nowcasting in southeastern Brazil: Analysis of a severe hailstorm case, *Weather and Forecasting*, 34,
535 1829–1848, <https://doi.org/10.1175/WAF-D-19-0070.1>, 2019.

536 Risi, C., Bony, S., and Vimeux, F.: Influence of convective processes on the isotopic composition ($\delta^{18}\text{O}$ and δD) of
537 precipitation and water vapor in the tropics: 2. Physical interpretation of the amount effect, *Journal of Geophysical Research*
538 *Atmospheres*, 113, 1–12, <https://doi.org/10.1029/2008JD009943>, 2008.

539 Risi, C., Bony, S., Vimeux, F., Chongd, M., and Descroix, L.: Evolution of the stable water isotopic composition of the rain
540 sampled along Sahelian squall lines, *Quarterly Journal of the Royal Meteorological Society*, 136, 227–242,
541 <https://doi.org/10.1002/qj.485>, 2010.

542 Risi, C., Noone, D., Frankenberg, C., and Worden, J.: Role of continental recycling in intraseasonal variations of continental
543 moisture as deduced from model simulations and water vapor isotopic measurements, *Water Resources Research*, 49, 4136–
544 4156, <https://doi.org/10.1002/wrcr.20312>, 2013.

545 Roberts, R. D. and Rutledge, S.: Nowcasting storm initiation and growth using GOES-8 and WSR-88D data, *Weather and*
546 *Forecasting*, 18, 562–584, [https://doi.org/10.1175/1520-0434\(2003\)018<0562:NSIAGU>2.0.CO;2](https://doi.org/10.1175/1520-0434(2003)018<0562:NSIAGU>2.0.CO;2), 2003.

547 Roca, R. and Fiolleau, T.: Extreme precipitation in the tropics is closely associated with long-lived convective systems,
548 *Communications Earth & Environment*, 1, 18, <https://doi.org/10.1038/s43247-020-00015-4>, 2020.

549 Romatschke, U. and Houze, R. A.: Characteristics of precipitating convective systems accounting for the summer rainfall of
550 tropical and subtropical South America, *Journal of Hydrometeorology*, 14, 25–46, <https://doi.org/10.1175/JHM-D-12-060.1>,
551 2013.

552 Rozanski, K., Sonntag, C., and Munnich, K. O.: Factors controlling stable isotope composition of European precipitation.,
553 *Tellus*, 34, 142–150, <https://doi.org/10.3402/tellusa.v34i2.10796>, 1982.

554 Rozanski, K., Araguás-Araguás, L., and Gonfiantini, R.: Isotopic Patterns in Modern Global Precipitation, 1–36,
555 <https://doi.org/10.1029/GM078p0001>, 1993.

556 Salati, E., Dall'Olio, A., Matsui, E., and Gat, J. R.: Recycling of water in the Amazon Basin: An isotopic study, *Water*
557 *Resources Research*, 15, 1250–1258, <https://doi.org/10.1029/WR015i005p01250>, 1979.

558 Sánchez-Murillo, R., Durán-Quesada, A. M., Birkel, C., Esquivel-Hernández, G., and Boll, J.: Tropical precipitation anomalies
559 and d-excess evolution during El Niño 2014–16, *Hydrological Processes*, 31, 956–967, <https://doi.org/10.1002/hyp.11088>,
560 2017.

561 Sánchez-Murillo, R., Durán-Quesada, A. M., Esquivel-Hernández, G., Rojas-Cantillano, D., Birkel, C., Welsh, K., Sánchez-
562 Llull, M., Alonso-Hernández, C. M., Tetzlaff, D., Soulsby, C., Boll, J., Kurita, N., and Cobb, K. M.: Deciphering key processes
563 controlling rainfall isotopic variability during extreme tropical cyclones, *Nature Communications*, 10, 1–10,

564 <https://doi.org/10.1038/s41467-019-12062-3>, 2019.

565 dos Santos, V., Gastmans, D., and Sánchez-Murillo, R.: Isotope and meteorologic database of high-frequency sampling of
566 convective rainfall events in Rio Claro, Brazil, <https://doi.org/10.17632/kk3gs8zn4s.1>, 2023.

567 Schmit, T. J., Griffith, P., Gunshor, M. M., Daniels, J. M., Goodman, S. J., and Lebar, W. J.: A closer look at the ABI on the
568 goes-r series, *Bulletin of the American Meteorological Society*, 98, 681–698, <https://doi.org/10.1175/BAMS-D-15-00230.1>,
569 2017.

570 Shapiro, S. S.; Wilk, M. B.: An analysis of variance test for normality (complete samples), *Biometrika*, 53, 591–611, 1965.

571 da Silva, G. J., Berg, E. C., Calijuri, M. L., dos Santos, V. J., Lorentz, J. F., and Carmo Alves, S. do: Aptitude of areas planned
572 for sugarcane cultivation expansion in the state of São Paulo, Brazil: a study based on climate change effects, *Agriculture,*
573 *Ecosystems & Environment*, 305, 107164, <https://doi.org/10.1016/j.agee.2020.107164>, 2021.

574 Siqueira, J. R. and Machado, L. A. T.: Influence of the frontal systems on the day-to-day convection variability over South
575 America, *Journal of Climate*, 17, 1754–1766, [https://doi.org/10.1175/1520-0442\(2004\)017<1754:IOTFSO>2.0.CO;2](https://doi.org/10.1175/1520-0442(2004)017<1754:IOTFSO>2.0.CO;2), 2004.

576 Siqueira, J. R., Rossow, W. B., Machado, L. A. T., and Pearl, C.: Structural characteristics of convective systems over South
577 America related to cold-frontal incursions, *Monthly Weather Review*, 133, 1045–1064, <https://doi.org/10.1175/MWR2888.1>,
578 2005.

579 Soderberg, K., Good, S. P., O’connor, M., Wang, L., Ryan, K., and Caylor, K. K.: Using atmospheric trajectories to model the
580 isotopic composition of rainfall in central Kenya, *Ecosphere*, 4, 1–18, <https://doi.org/10.1890/ES12-00160.1>, 2013.

581 Stein, A. F., Draxler, R. R., Rolph, G. D., Stunder, B. J. B., Cohen, M. D., and Ngan, F.: NOAA’s hysplit atmospheric transport
582 and dispersion modeling system, *Bulletin of the American Meteorological Society*, 96, 2059–2077,
583 <https://doi.org/10.1175/BAMS-D-14-00110.1>, 2015.

584 Steiner, M. and Smith, J. A.: Convective versus stratiform rainfall: An ice-microphysical and kinematic conceptual model,
585 *Atmospheric Research*, 47–48, 317–326, [https://doi.org/10.1016/S0169-8095\(97\)00086-0](https://doi.org/10.1016/S0169-8095(97)00086-0), 1998.

586 Sun, C., Shanahan, T. M., and Partin, J.: Controls on the Isotopic Composition of Precipitation in the South-Central United
587 States, *Journal of Geophysical Research: Atmospheres*, 124, 8320–8335, <https://doi.org/10.1029/2018JD029306>, 2019.

588 Sun, C., Tian, L., Shanahan, T. M., Partin, J. W., Gao, Y., Piatrunia, N., and Banner, J.: Isotopic variability in tropical cyclone
589 precipitation is controlled by Rayleigh distillation and cloud microphysics, *Communications Earth & Environment*, 3,
590 <https://doi.org/10.1038/s43247-022-00381-1>, 2022.

591 Taupin, J.-D., Gallaire, R., and Arnaud, Y.: Analyses isotopiques et chimiques des précipitations sahélienne de la région de
592 Niamey au Niger: implications climatologiques, *Hydrochemistry*, 151–162, 1997.

593 Thurnherr, I. and Aemisegger, F.: Disentangling the impact of air – sea interaction and boundary layer cloud formation on
594 stable water isotope signals in the warm sector of a Southern Ocean cyclone, *Atmospheric Chemistry and Physics*, 22, 10353–
595 10373, <https://doi.org/10.5194/acp-22-10353-2022>, 2022.

596 Torri, G.: On the Isotopic Composition of Cold Pools in Radiative-Convective Equilibrium, *Journal of Geophysical Research:*
597 *Atmospheres*, 126, 1–20, <https://doi.org/10.1029/2020JD033139>, 2021.

598 Tremoy, G., Vimeux, F., Soumana, S., Souley, I., Risi, C., Favreau, G., and Oï, M.: Clustering mesoscale convective systems
599 with laser-based water vapor δ 18 O monitoring in Niamey (Niger), *Journal of Geophysical Research: Atmospheres*, 119,
600 5079–5103, <https://doi.org/10.1002/2013JD020968>, 2014.

601 Uijlenhoet, R.: Raindrop size distributions and radar reflectivity–rain rate relationships for radar hydrology, *Hydrology and*
602 *Earth System Sciences*, 5, 615–628, <https://doi.org/10.5194/hess-5-615-2001>, 2001.

603 Vila, D. A., Machado, L. A. T., Laurent, H., and Velasco, I.: Forecast and tracking the evolution of cloud clusters (ForTraCC)
604 using satellite infrared imagery: Methodology and validation, *Weather and Forecasting*, 23, 233–245,
605 <https://doi.org/10.1175/2007WAF2006121.1>, 2008.

606 de Vries, A. J., Aemisegger, F., Pfahl, S., and Wernli, H.: Stable water isotope signals in tropical ice clouds in the West African
607 monsoon simulated with a regional convection-permitting model, *Atmospheric Chemistry and Physics*, 22, 8863–8895,
608 <https://doi.org/10.5194/acp-22-8863-2022>, 2022.

609 Worden, J., Noone, D., Bowman, K., Beer, R., Eldering, A., Fisher, B., Gunson, M., Goldman, A., Herman, R., Kulawik, S.
610 S., Lampel, M., Osterman, G., Rinsland, C., Rodgers, C., Sander, S., Shephard, M., Webster, C. R., and Worden, H.:
611 Importance of rain evaporation and continental convection in the tropical water cycle, *Nature*, 445, 528–532,
612 <https://doi.org/10.1038/nature05508>, 2007.

613 Worden, S., Fu, R., Chakraborty, S., Liu, J., and Worden, J.: Where Does Moisture Come From Over the Congo Basin?,
614 *Journal of Geophysical Research: Biogeosciences*, 126, 1–14, <https://doi.org/10.1029/2020JG006024>, 2021.

615 World Meteorological Organization: WMO Atlas of Mortality and Economic Losses From Weather , Climate and Water
616 Extremes (1970-2019), Geneva 2, Switzerland, 90 pp., 2021.

617 Zilli, M. T., Carvalho, L. M. V., Liebmann, B., and Silva Dias, M. A.: A comprehensive analysis of trends in extreme
618 precipitation over southeastern coast of Brazil, *International Journal of Climatology*, 37, 2269–2279,
619 <https://doi.org/10.1002/joc.4840>, 2017.

620 Zwart, C., Munksgaard, N. C., Protat, A., Kurita, N., Lambrinidis, D., and Bird, M. I.: The isotopic signature of monsoon
621 conditions, cloud modes, and rainfall type, *Hydrological Processes*, 32, 2296–2303, <https://doi.org/10.1002/hyp.13140>, 2018.

622

623

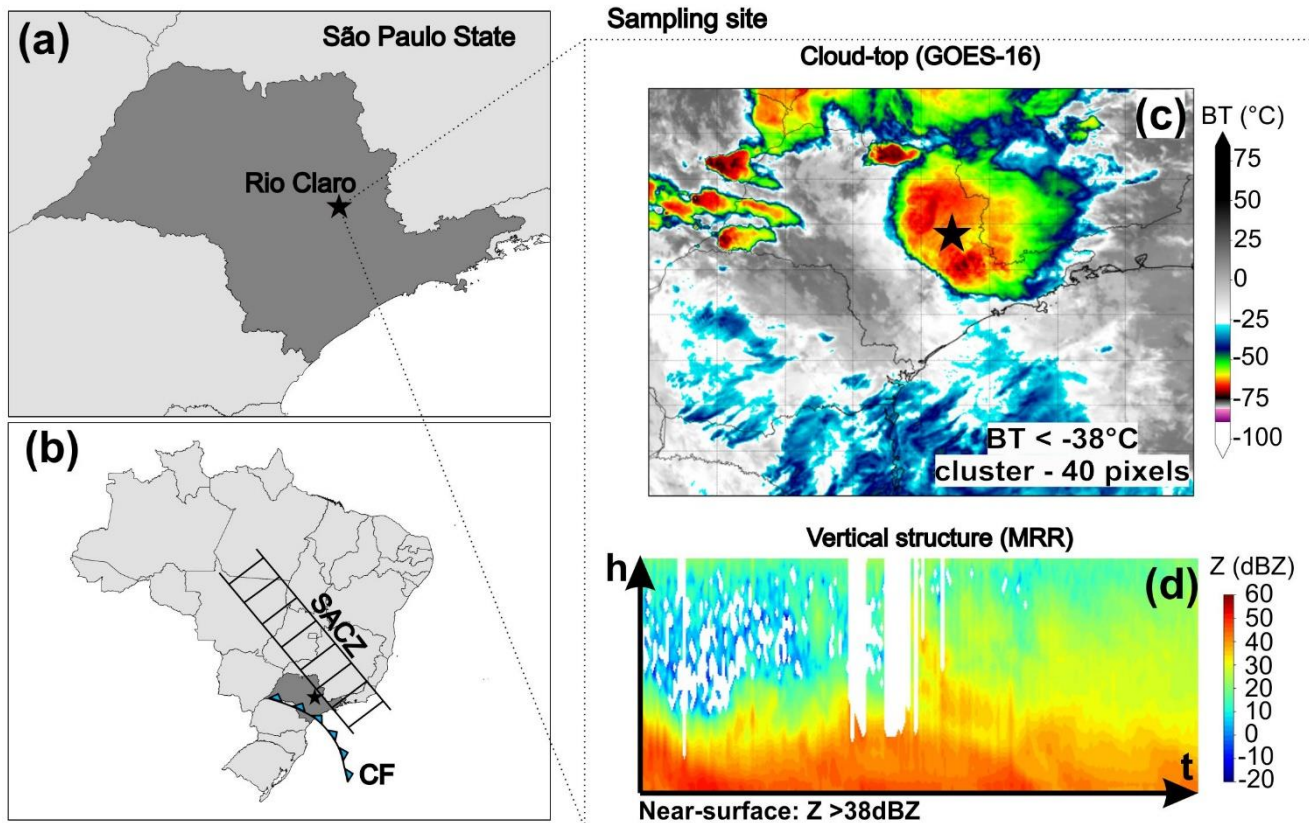
624

625

Table 1. Summarizing overall convective rainfall events, isotope and meteorological parameters

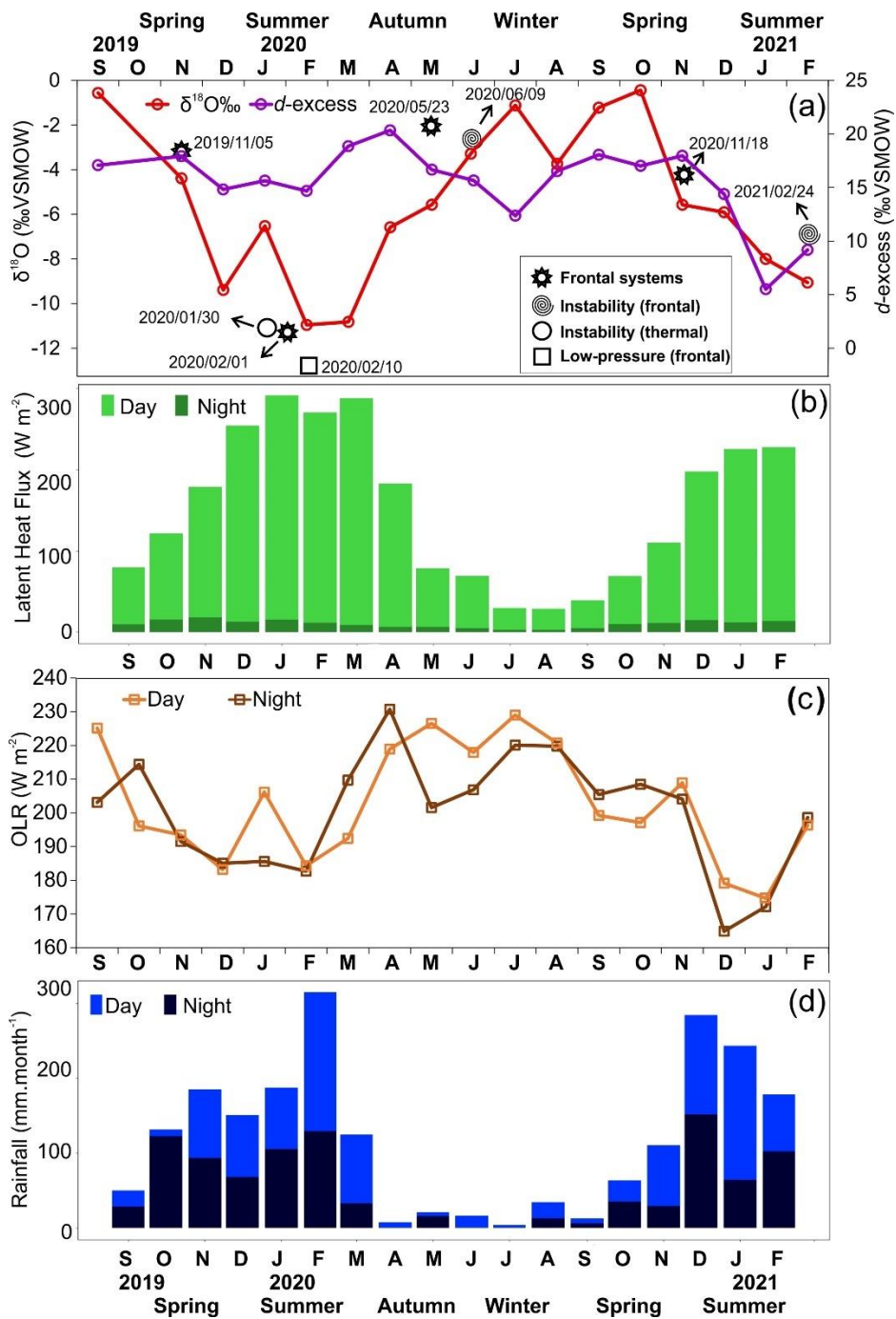
Season		Spring		Autumn			Summer		
Data		05/11/2019	18/11/2020	09/06/2020	23/05/2020	30/01/2020	10/02/2020	01/02/2020	24/02/2021
Number of samples		21	8	12	4	6	18	5	16
Duration		82	141	96	131	23	86	18	55
$\delta^{18}\text{O}$	Median	-3.1	-4.2	-3.4	-2.9	-10.0	-13.9	-10.4	-6.8
	Weighted average	-3.0	-4.2	-2.7	-2.9	-10.0	-13.4	-11.1	-7.2
$\delta^2\text{H}$	Median	0.8	-13.7	-5.6	-6.9	-64.4	-92.0	-73.5	-44.8
	Weighted average	-1.2	-14.9	-4.9	-6.8	-63.9	-90.4	-75.0	-47.2
<i>d</i>-excess	Median	22.9	19.7	17.3	16.3	15.7	17.5	13.4	7.2
	Weighted average	23.3	19.1	17.3	16.5	16.5	16.7	14.2	11.1
Automatic Weather Station	Rain rate	0.4	0.2	0.3	0.0	0.4	0.5	0.6	0.5
	RH	96	86	95	87	93	97	93	86
	T	21	20	19	19	23	22	23	21
	Tdw	20	17	18	17	21	21	21	18
	LCL	146	489	168	449	247	93	253	468
Micro Rain Radar	Z	46	38	42	33	38	41	39	35
	w	8	7.1	7.7	6.6	6.6	6.7	7.1	7.1
GOES-16	BT	-63	-63	-50	-56	-53	-39	-60	-51

Duration (minutes); Isotopes parameters (‰); Median values of meteorological variables: Rain rate ($\text{mm}\cdot\text{min}^{-1}$), Relative Humidity – (RH %), Temperature (T °C), Dew Temperature (Tdw °C), Lifting Condensation Level (LCL meters), Reflectivity (Z dBZ), Vertical Velocity ($\text{m}\cdot\text{s}^{-1}$) and Brightness temperature (BT °C).



630

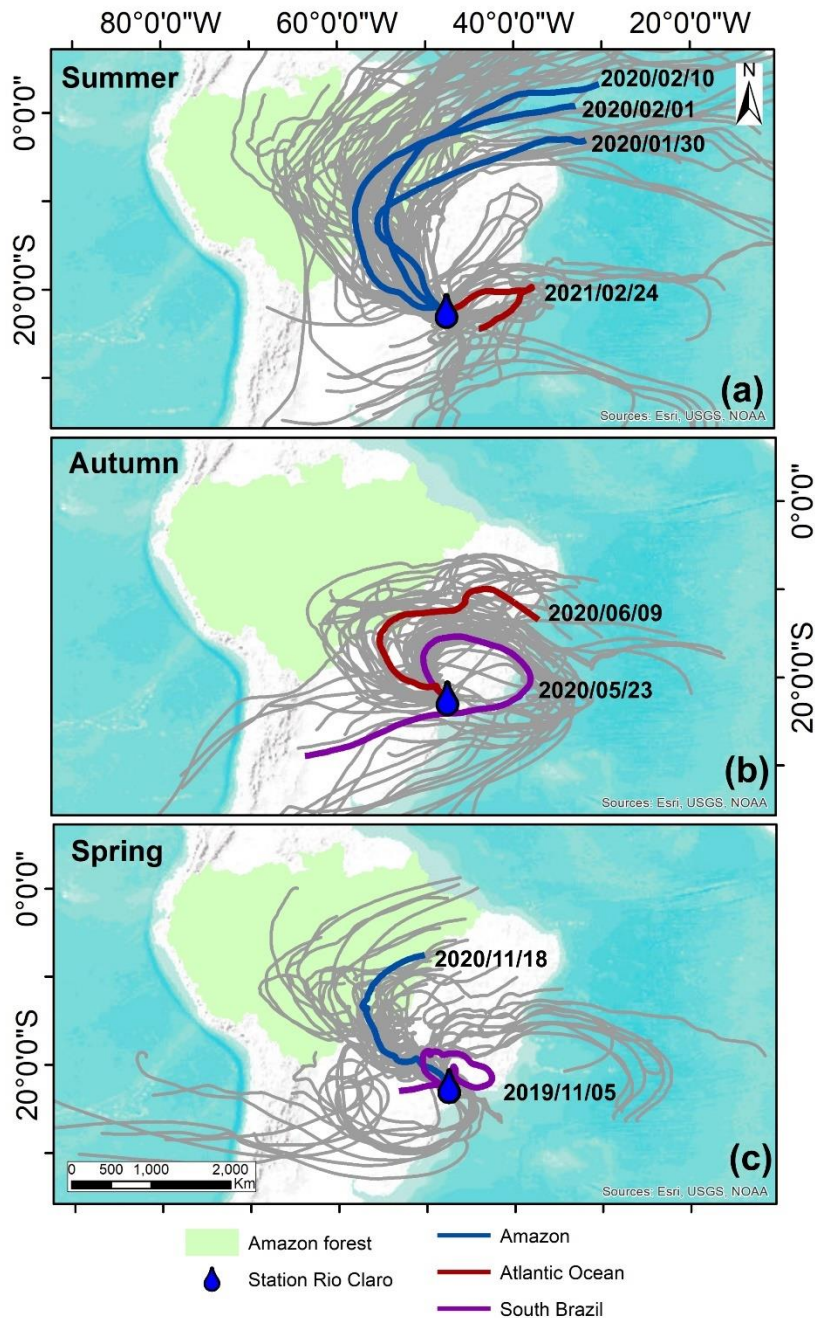
Figure 1. Regional and local context of study area. (a) Localization of sampling site in Rio Claro (black star) (b) regional synoptic context across Brazil and main weather systems (CF – cold front and SACZ – Southern Atlantic Convergence Zone). (c) GOES-16 satellite imagery of convective rainfall (d) Micro Rain Radar (MRR) image of convective rainfall.



635

Figure 2. Seasonal variation of isotope and convective parameters. (a) Temporal distribution of monthly $\delta^{18}\text{O}$ and d -excess values during study period, with aggregated median of $\delta^{18}\text{O}$ values for high-frequency convective rainfall events (b) AQUA/AIRS latent heat flux. (c) MERRA-2 outgoing longwave radiation (monthly averaged daytime and night-time data) (d) monthly rainfall amounts at Rio Claro separated into day and night fraction (no rainfall types distinguished). The black symbol indicates weather systems described in section 3.1. The monthly isotopic composition used in this figure was collected by the first authors of the article and determined by the UNESP laboratory, following the same procedures mentioned in section 2.2.

640



645 **Figure 3.** Ten-day backward trajectories arriving at Rio Claro station of eight convective events. (a) Summer, (b) Autumn and (c) Spring. Twenty-seven ensembles are grey lines, and the mean trajectory is the colors lines. The colours of the mean trajectories indicate the origin of air masses. The authors used trivial information, the borders of the countries and the ocean provided by the ESRI base map.

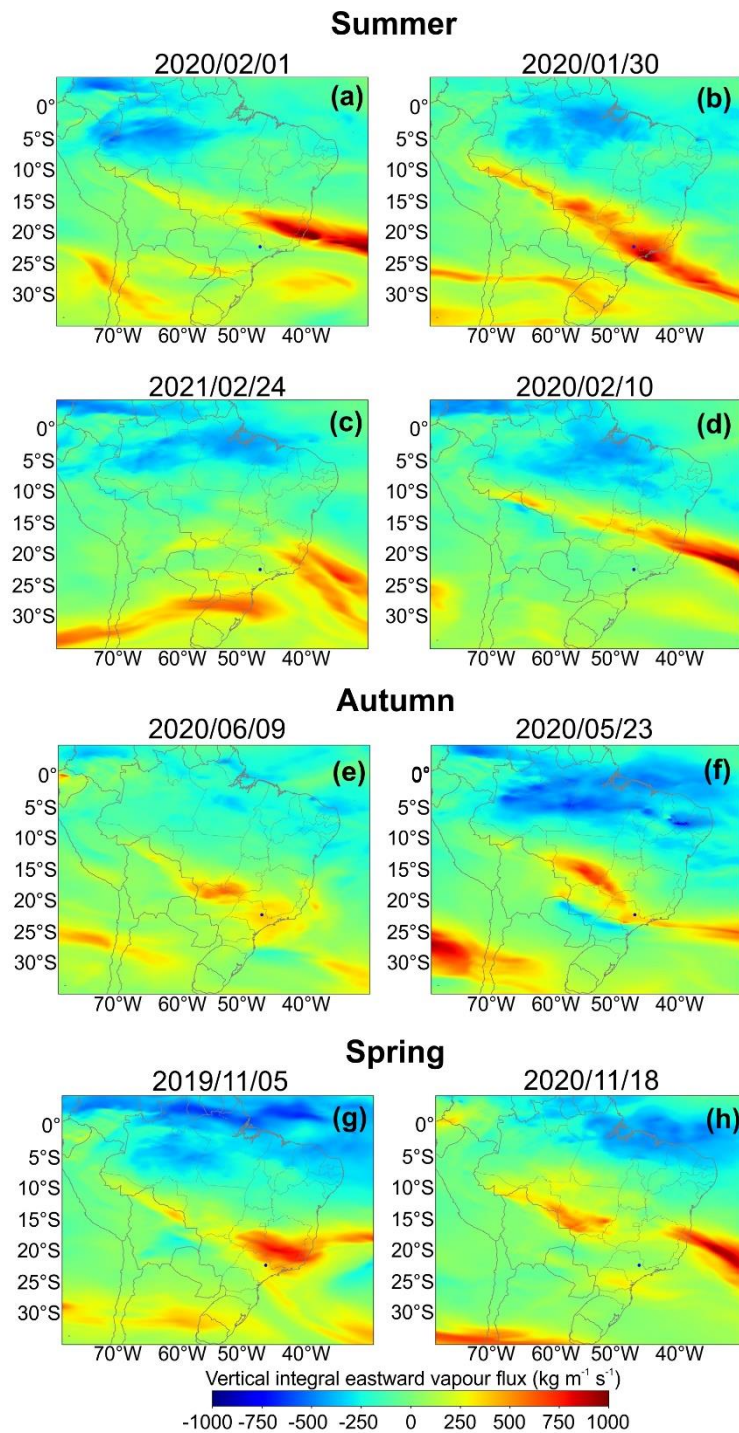


Figure 4. ERA-5 vertical integral of eastward water vapor flux. (a, b, c, d) summer convective events (e, f) autumn and (g, h) spring aggregated. The maps corresponded to the days when convective rainfall events occurred. Positive values indicate the direction of moisture vapor flux from left to right, and negative values from right to left.

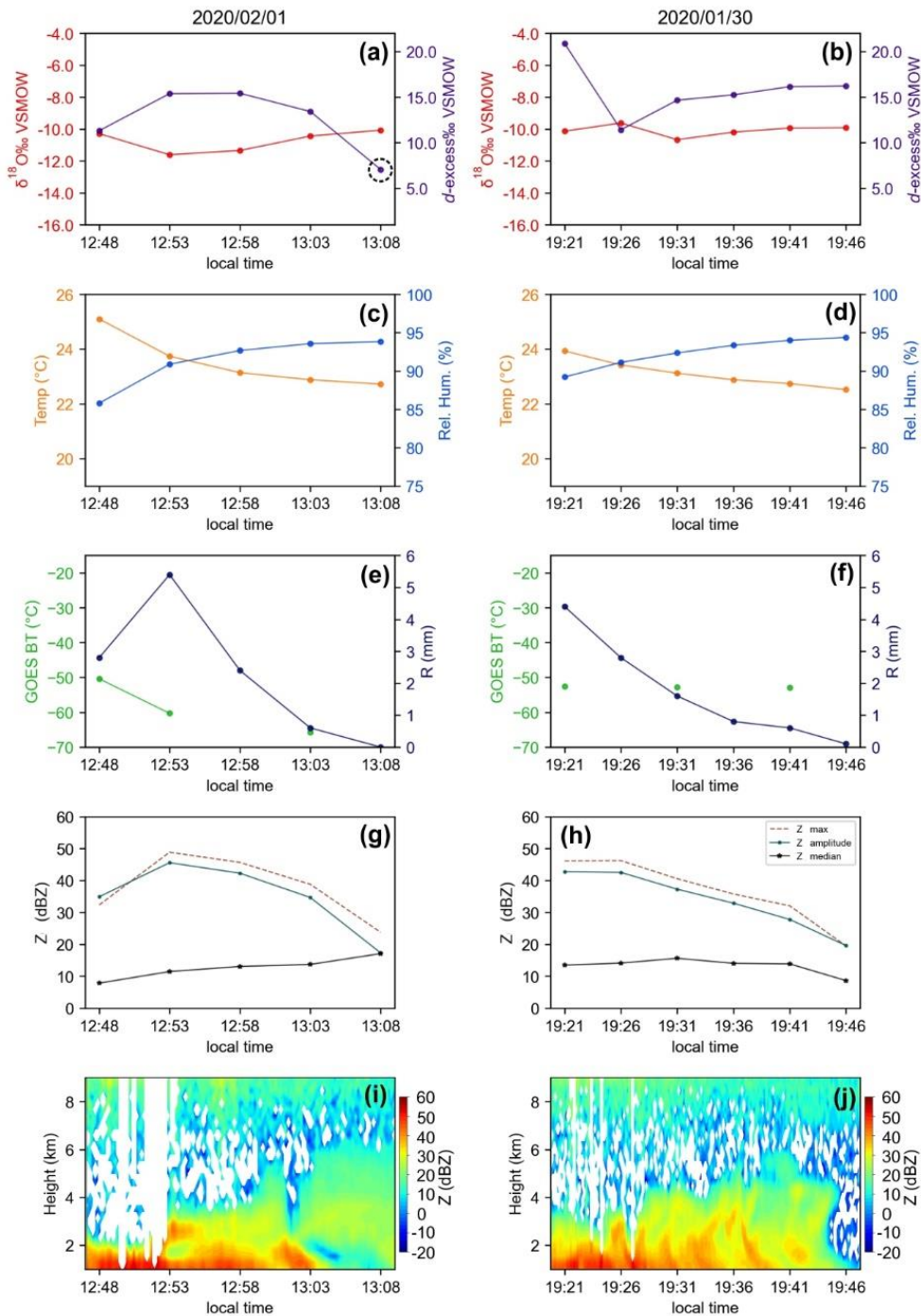


Figure 5. Summer intra-events. (a, b) $\delta^{18}\text{O}$ (red lines) and $d\text{-excess}$ (purple lines) (c, d) Temperature (orange lines) and Relative Humidity (blue lines) (e, f) brightness temperature (BT – green bars) and rainfall amount (blue lines) (g, h) Reflectivity parameters, Z maximum (red lines), Z amplitude (green lines) and Z median (black lines) (i, j) radar reflectivity of Micro Rain Radar. The black dotted cycle refers to the low $d\text{-excess}$ value.

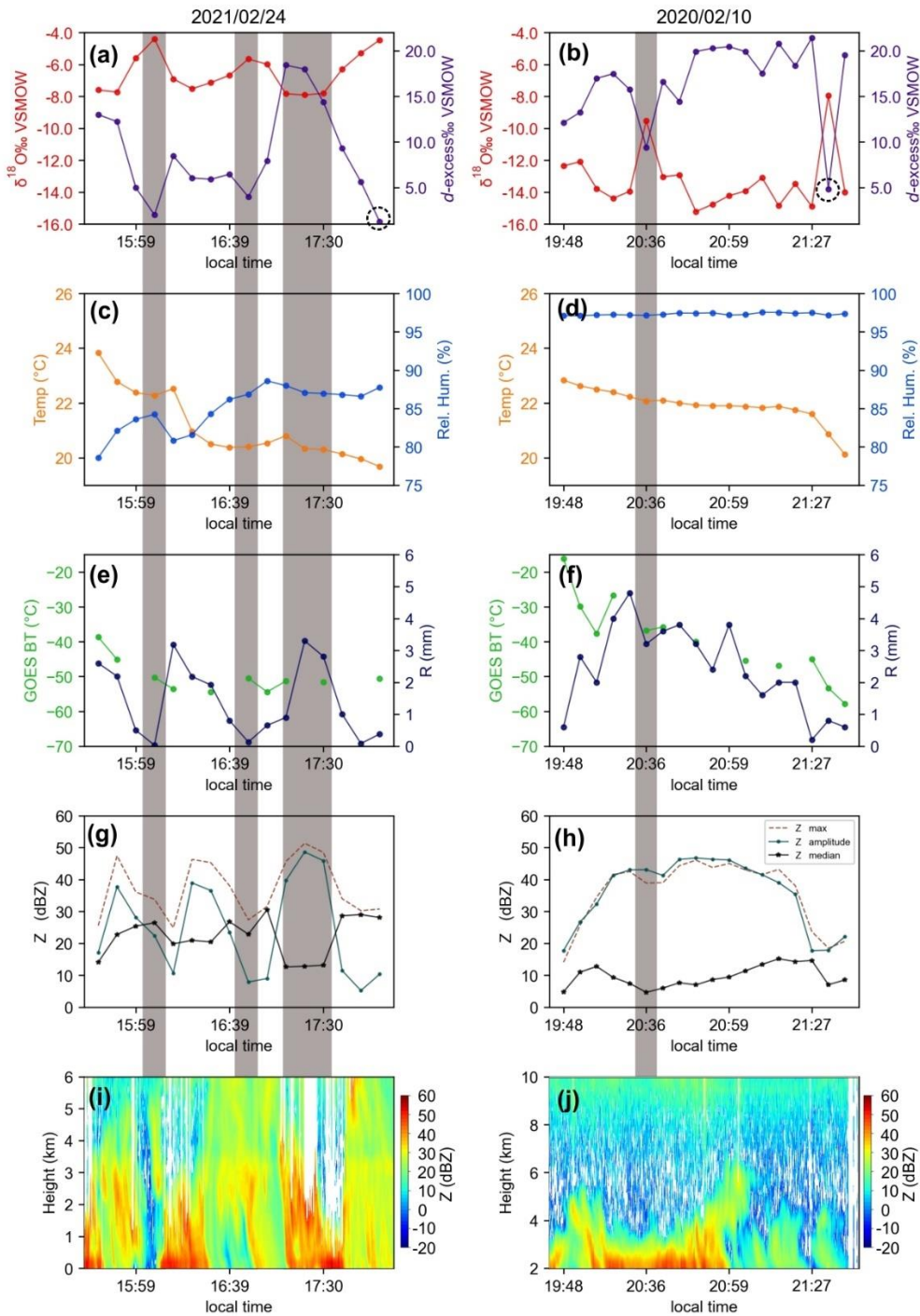


Figure 6. Summer intra-events. Refer to Fig. 5 for legend description.

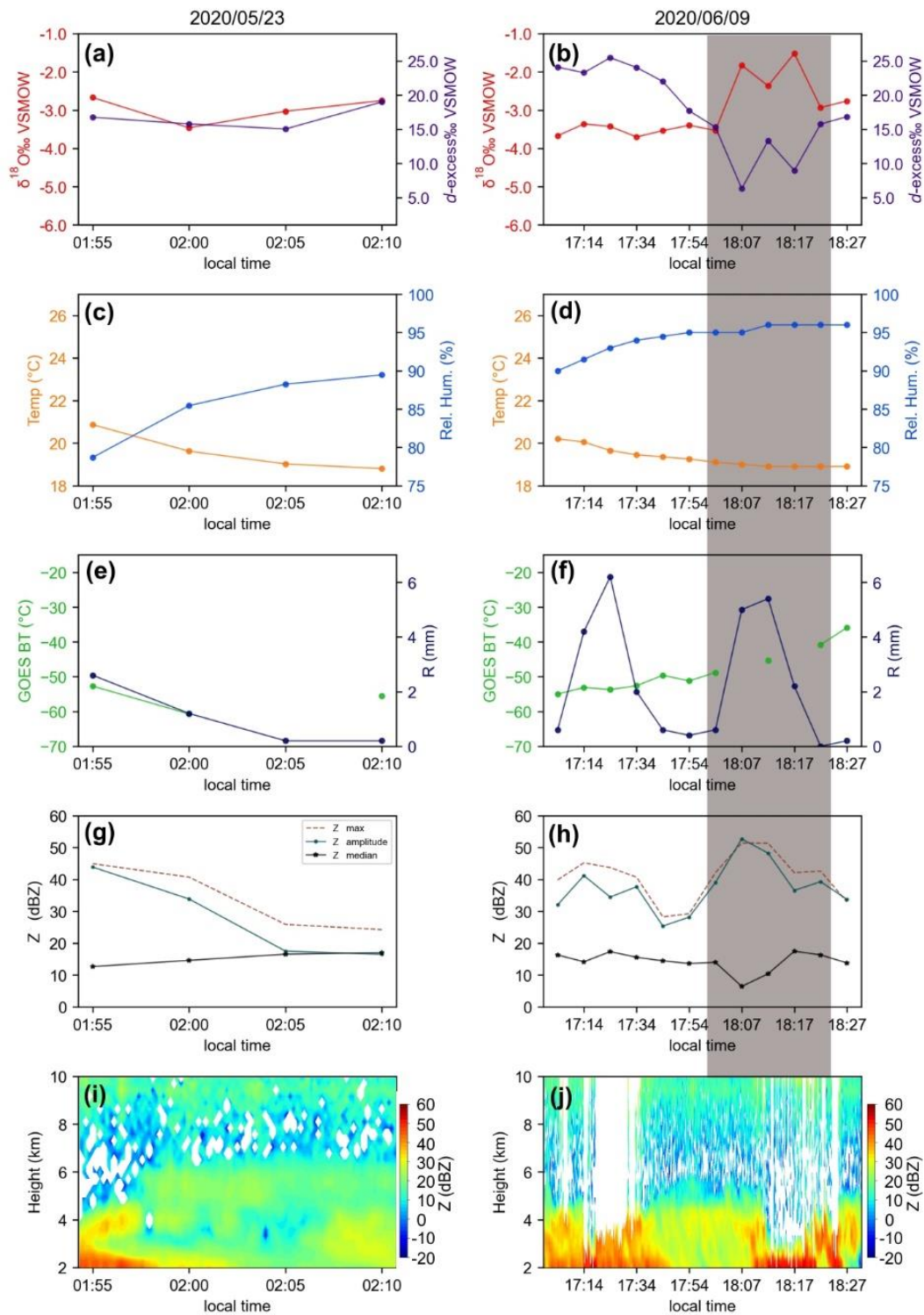


Figure 7. Autumn intra-events. Refer to Fig. 5 for legend description.

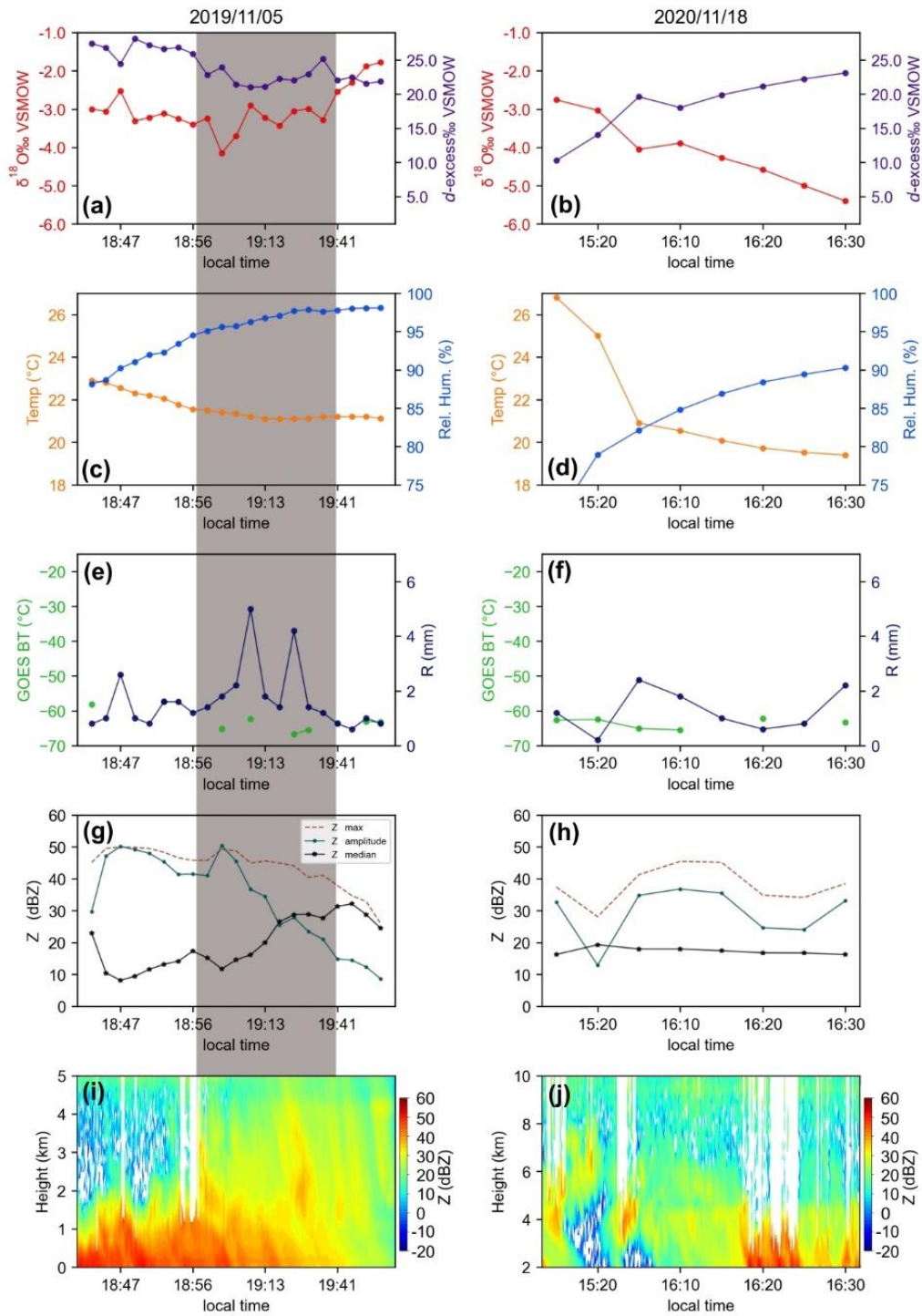


Figure 8. Spring intra-events. Refer to Fig. 5 for legend description.